# Identification and Dynamic Model of a Bipedal Robot With a Cable-Differential-Based Compliant Drivetrain

Hae-Won Park, Koushil Sreenath, Jonathan W. Hurst and J.W. Grizzle

***Abstract*—This research identifies an eleven degree of freedom dynamic model of MABEL, a new robot for the study of bipedal walking and running. Model parameters are identified on the basis of fourteen angles measured by encoders and the commanded torque of the robot's four independent actuators. The identification process is modular and begins with the cable-driven transmission mechanism of the robot. By blocking an appropriate pulley, the springs that are part of the transmission can be removed from the initial portion of the identification process. Furthermore, by selectively connecting and disconnecting cables in the transmission, experiments are designed for each actuated coordinate in order to determine inertias, friction coefficients, motor constants, and power amplifier biases of the transmission system. With the identified transmission model and estimates of the inertial parameters of the torso and legs from a CAD package, *a priori* estimates of the robot's overall dynamic model can be constructed. These *a priori* estimates are initially validated by comparing predicted response of the combined legs and transmission system to experimental data excited by common torque commands. At this point, the compliant elements in the transmission are brought back into the system and are identified with a set of static experiments. Specifically, spring stiffness is estimated from the spring torques and deflections. A second unplanned source of compliance is accounted for next. This compliance arises when the cables connecting the pulleys in the transmission stretch under heavy loads. The overall model of the robot is validated through a hopping experiment that excites all of the dynamics of the model.**

***Index Terms*—Compliance, Dynamics, Legged Robots, Identification**

## I. Introduction

The primary objective of the research reported in this paper is to identify parameters which appear in a dynamic model of MABEL, a new robot for the study of bipedal walking and running at the University of Michigan's EECS Department; see Fig. 1. MABEL uses a novel assembly of cable differentials, springs, and hard stops to achieve a low-friction, compliant drivetrain, with the objective of improving the energy efficiency and robustness of bipedal locomotion, both in steady state operation and in responding to disturbances [1], [2]. The parameters we seek to identify correspond to inertial parameters of the pulleys comprising the differentials, motor rotor inertias, various friction coefficients, spring constants, and power amplifier biases.

Hae-Won Park is with the Mechanical Engineering Department, University of Michigan, Ann Arbor, MI, 48109-2125, USA, parkhw@umich.edu

Koushil Sreenath and J. W. Grizzle are with the Control Systems Laboratory, Electrical Engineering and Computer Science Department, University of Michigan, Ann Arbor, MI 48109-2122, USA, koushils@umich.edu.

Jonathan W. Hurst is with the School of Mechanical, Industrial, and Manufacturing Engineering, Oregon State University, Corvallis, OR 97331-6001, USA, jonathan.hurst@oregonstate.edu.

This work is supported by NSF grant ECS-909300.

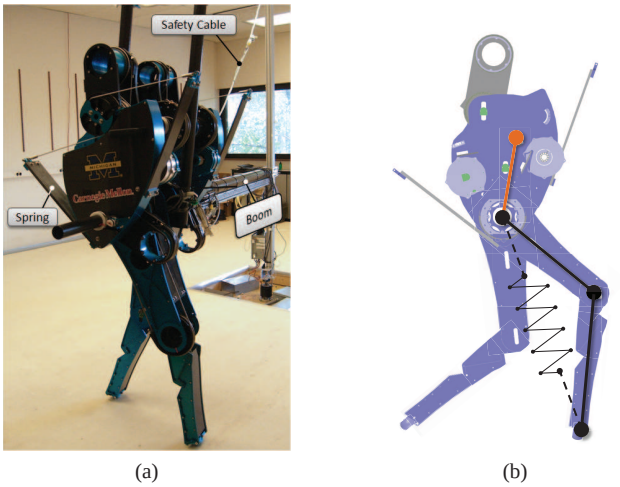


(a) (b)

Fig. 1: (a) MABEL, a bipedal robot for walking and running. The shin and thigh are each 50 cm long, making the robot one meter tall at the hip. The overall mass is 60 kg, excluding the boom. The robot's drivetrain incorporates unilateral springs for shock absorption and energy storage.
(b) The robot's drivetrain uses a set of differentials and a spring to create a virtual pneumatic leg with compliance.

A secondary objective of this paper is to present a dynamic model of the robot's drivetrain. With the drivetrain model in hand, developing the dynamic model of the overall biped becomes a standard exercise in Lagrangian mechanics [3], [4]. To evaluate the validity of the overall dynamic model of the robot, a dynamic hopping experiment is performed where the robot repeatedly jumps off the floor with both legs and lands in a stable manner.

The problem of parameter identification for robot models has been well studied in [5], [6], [7], [8], [9], [10]. Most results are based on the analysis of the input-output behavior of the robot during a planned motion, with the parameter values obtained by minimizing the difference between a function of the measured robot variables and a mathematical model [7]. A very clear illustration of this approach is presented in [5] for the identification of parameters in industrial manipulators. The standard rigid-body model is rewritten in a parametric form which is linear in the unknown parameters, $\tau = \phi(q, \dot{q}, \ddot{q})\theta$, where $q$, $\dot{q}$, $\ddot{q}$ are the position, velocities, and accelerations of the joints, $\tau$ is the vector of joint torques, $\theta$ is the unknown parameter vector, and $\phi$ is the regressor matrix. Optimization is used to define trajectories that enhance the condition number of $\phi$, and these trajectories are then executed on the robot. Weighted least-squares estimation is applied next to extract parameters, and the parameters are in turn validated by torque

prediction. This approach requires acceleration, which typically must be estimated numerically from measured position. Very careful signal processing is therefore required to obtain accurate parameter estimates. Research in [11] also exploited a linear-in-parameter form of the model. First, the gravitational parameters were estimated on the basis of a static experiment, and then inertia and friction parameters are obtained by least square fit to experimental data from a dynamic experiment. Other researchers have sought to obtain efficient algorithms for parameter estimation of serial robots by determining a minimum set of inertial parameters in a mathematical model [12], [13].

An alternative approach has been explored in [8], which exploited force and torque sensor measurements to avoid estimating acceleration. The model was represented in Newton-Euler form, and a six element wrench at the robot's wrist was expressed in a form linear in the unknown parameters. Force and torque at the wrist were obtained directly through force and torque sensors, and parameter estimation was accomplished from this data without the need for acceleration. Another class of methods has been presented in [9], which used an energy-based model that requires velocity and position variables, but does not require acceleration. This method, however, relies on the integration of the input torques and the joint velocities to compute energy, which is problematic if estimated torque is corrupted by a bias. Reference [10] presented the idea of designing separate experiments for estimating different types of parameters involving the inertial forces, centrifugal coupling forces, friction forces, and gravity forces. The estimated parameters from each identification procedure were isolated to one of these four forces at a time.

In this paper, we identify the parameters in a dynamic model of MABEL. Parameter identification for MABEL is a challenging task for the following reasons: First, MABEL has a limited number of sensors, including only position encoders at the motors and joints, and lacks any force or torque sensors. Second, actuator characteristics are poorly known. The motors used in MABEL are custom made BLDC (brushless direct current) motors which are only manufactured on demand. Hence, important motor characteristics such as rotor inertia, torque constant, and mechanical time constants are not precisely measured and verified by the manufacturer. Identification of those parameters must therefore be included in the system identification procedure. In combination with power amplifiers from a different manufacturer, the motors exhibited some directional bias. Complicating matters further, this bias varies among individual amplifier-motor pairs. Consequently, the amplifier bias must be considered in the system identification process. Another issue that affects our approach to parameter identification is that the choice of exciting trajectory is restricted due to limitations of MABEL's work space. For example, a constant velocity experiment for estimating friction coefficients is not feasible for MABEL because the maximum rotation of any joint is less than $180°$. Finally, because MABEL has many degrees of freedom, actuating all of them at once would lead to a large number of unknown parameters. For this reason, we take advantage of the modular nature of the robot to design experiments that allow us to sequentially build the model element by element. We use commanded motor torques as inputs, and motor and joint position encoders as outputs, and extract model parameters on the basis of those signals. Due to the quantization error of the magnetic encoders, it is difficult to get accurate acceleration signals by differentiating encoder position signals. Hence, we seek to extract parameters without calculating acceleration from position data.

The paper is organized as follows: Section II describes the robot being studied. Section III briefly overviews the system identification process. Section IV, Section V, Section VI, and Section VII cover the identification of the transmission mechanism, the legs, the torso, and the compliance, respectively. Finally, Section VIII validates the overall dynamic model through a hopping experiment.

## II. Mechanism Overview

MABEL, shown in Fig. 1, is a planar bipedal robot comprised of five links assembled to form a torso and two legs. A novel feature of the robot is that it is constructed from two monopods joined at the hip. By removing six bolts, half of MABEL's torso and one leg can be removed, yielding a monopod. In fact, the monoped hopping robot "Thumper" at Oregon State University is literally the left half of MABEL [14].

In MABEL, the actuated degrees of freedom of each leg do not correspond to the knee and the hip angles (the hip angle being the relative angle between the torso and thigh). Instead, for each leg, a collection of differentials is used to connect two motors to the hip and knee joints in such a way that one motor controls the angle of the virtual leg (denoted hereafter by LA, where LA stands for Leg Angle) consisting of the virtual line connecting the hip to the toe, and the second motor is connected, in series with a spring, to the length of the virtual leg (denoted hereafter by LS, where LS stands for Leg Shape). The conventional bipedal robot coordinates and MABEL's unique set of actuated coordinates are depicted in Fig. 2; they are related by the following equations

$$\begin{aligned} q_{\mathrm{LA}} &= \frac{1}{2}\left(q_{\mathrm{Thigh}} + q_{\mathrm{Shin}}\right) \\ q_{\mathrm{LS}} &= \frac{1}{2}\left(q_{\mathrm{Thigh}} - q_{\mathrm{Shin}}\right). \end{aligned} \tag{1}$$

Roughly speaking, the rationale for this design is that it makes the robot a hybrid of RABBIT, a robot that walks extremely well, but never achieved a stable running gait [15], and a Raibert Hopper, a robot that "runs" remarkably well [16]. The springs in MABEL serve to isolate the reflected rotor inertia of the leg-shape motors[1] from the impact forces at leg touchdown and to store energy in the compression phase of a running gait, when the support leg must decelerate the downward motion of the robot's center of mass; the energy stored in the spring can then be used to redirect the center of mass upwards for the subsequent flight phase, when both legs will be off the ground. Both of these properties (shock isolation and energy storage) enhance the energy efficiency of running

[1]Inertial load of the motor rotor seen from the joint end.

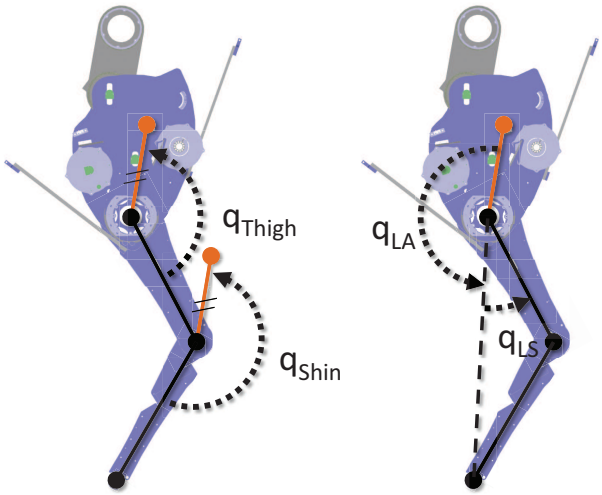


Fig. 2: Conventional bipedal robot coordinates and MABEL's unique coordinates. Counter clockwise direction is positive

and reduce overall actuator power requirements [17], [2], [1]. This is also true for walking on flat ground, but to a lesser extent, due to the lower forces at leg impact and the reduced vertical travel of the center of mass. The robotics literature strongly suggests that shock isolation and compliance will be very useful for walking on uneven terrain [18], [19], [20], [21], [22], [23], [24].

### A. Robot Body

MABEL consists of five links: a torso, two thighs, and two shins. The robot is attached to a boom to constrain the robot's path to the surface of a sphere as shown in Fig. 3. The robot's motion is tangential to the sphere centered in the middle of the laboratory. With a sufficiently long boom, its motion is similar to that of a perfectly planar robot walking in a straight line.

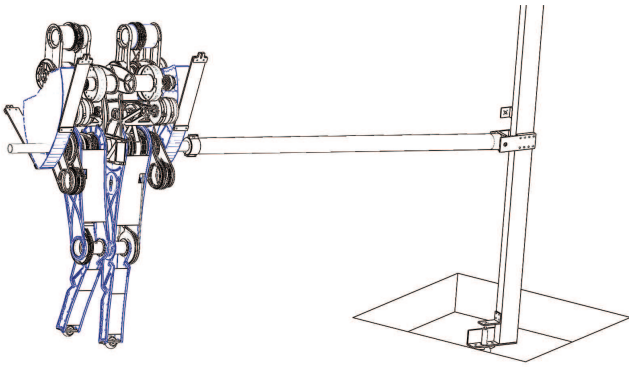

Fig. 3: Boom constraining MABEL's motion to the surface of a sphere, which approximates 2D planar motion. The central tower is supported on a slip ring through which power and digital communication lines (E-stop line and ethernet lines) are passed.

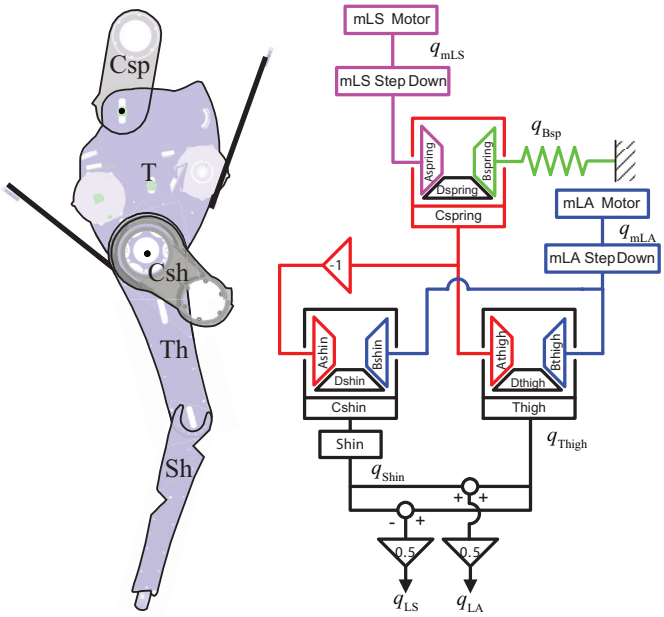


(a) (b)

Fig. 4: (a) Links comprising MABEL. Csp, T, Csh, Th, Sh stand for $C_{Spring}$, $Torso$, $C_{Shin}$, $Thigh$, and $Shin$, respectively. (b) Transmission mechanism in MABEL and the coordinates for the transmission mechanism. The mechanism consists of spring, thigh, and shin differentials. The spring differential realizes a serial connection between the leg-shape motor and the spring. The thigh differential realizes movement of the thigh link in the leg and the shin differential moves the shin link. More details on gear ratios are provided in Fig. 6 and Fig. 7.

### B. Transmission Mechanism

The transmission mechanism for each half of the robot consists of three cable differentials, labeled the spring, thigh, and shin differentials, respectively, and a spring, as shown in Fig. 4b. Two differentials at the hip, the thigh and shin differentials, serve to translate shin angle and thigh angle into leg length and leg angle. Thus, the electric motors control the leg angle and the leg length. The spring differential serves to apply spring torques in series between the leg length so the resulting system behaves approximately like a pogo stick. $C_{Thigh}$ and $C_{Shin}$ in Fig. 4b are attached to the thigh and shin links, respectively. The $B_{Thigh}$ and $B_{Shin}$ pulleys are both connected to the leg-angle motor. The $A_{Thigh}$ and $A_{Shin}$ pulleys are connected to the $C_{Spring}$ pulley, which is the output pulley of the spring differential. The spring on each side of the robot is implemented via two fiberglass plates connected in parallel to the differentials via cables; see Fig. 1. As explained in more detail in Section VII-A, the springs are unilateral (can compress in only one direction).

Cable differentials are used instead of the more standard gear differentials depicted in Fig. 5. In part, this choice was made in order to achieve low friction and backlash, and low mass in the legs. Although cable differentials and gear differentials have different assemblies, they work in the same

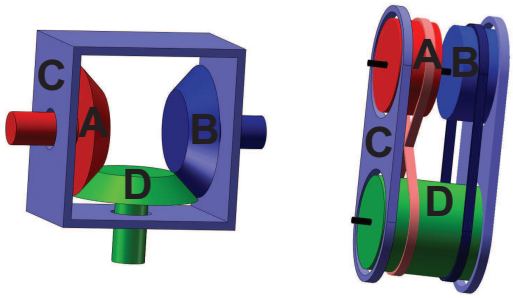


Fig. 5: Two versions of a differential mechanism. **Left**: Gear Differential, **Right**: Cable Differential. The A, B, C, and D pulleys of each mechanism operate in the same manner.

manner. There is a special connection of three components (labeled $A$, $B$, and $C$), and an internal, unobserved idler ($D$). The kinematic equations for a differential are given by $\frac{A+B}{2} = C$ and $\frac{A-B}{2} = D$, assuming the gear ratios are all equal. The $A$ and $B$ components are constrained such that the average motion of the two is equal to the motion of the $C$ component. Consequently, $A$ and $B$ can move in opposite directions if $C$ is held stationary, and the motion of $C$ will be half of $A$ if $B$ is held stationary. In MABEL's transmission mechanism, $A$ and $B$ are used as inputs to the differential, and $C$ is used as an output. In the following, $A_{Shin}$, $B_{Shin}$ and $C_{Shin}$ refer to the $A$, $B$ and $C$ components of the shin differential; similar nomenclature is used for the other two differentials.

Fig. 6 and Fig. 7 describe how this transmission works when $q_{\mathrm{LA}}$ or $q_{\mathrm{LS}}$ is actuated, while the other link is held fixed. As part of the description, directions and gear ratios are specified.

The path from spring torque (displacement) to rotation in $q_{\mathrm{LS}}$ is very similar. Because the transmission is linear, the net motion in $q_{\mathrm{LS}}$ from the leg-shape motor and the spring is the sum of the individual motions.

### C. Notation for naming the parameters and variables

For later use, we define following index sets.

$$\mathcal{I} = \{\mathrm{mLS_L},\ \mathrm{mLA_L},\ \mathrm{mLS_R},\ \mathrm{mLA_R}\}, \tag{2}$$

where the subscripts L and R mean left and right, mLS means motor leg shape, and mLA means motor leg angle; see Fig. 4b. For the links, we define the index set

$$\mathcal{L} = \{\mathrm{T}, \mathrm{Csp}, \mathrm{Th}, \mathrm{Sh}, \mathrm{Csh}, \mathrm{Boom}\}, \tag{3}$$

where, T, Csp, Th, Sh, Csh, and Boom represent $Torso$, $C_{Spring}$, $Thigh$, $Shin$, $C_{Shin}$, and $Boom$, respectively, as depicted in Fig. 4a. For the transmission mechanism, we define the index set

$$\begin{aligned}\mathcal{T} = \{&\mathrm{Asp}, \mathrm{Bsp}, \mathrm{Dsp}, \mathrm{Ath}, \mathrm{Bth}, \mathrm{Dth}, \mathrm{Ash},\\ &\mathrm{Bsh}, \mathrm{Dsh}, \mathrm{mLSsd}, \mathrm{mLAsd}, \mathrm{mLS}, \mathrm{mLA}\},\end{aligned} \tag{4}$$

where capital letters A, B, and D correspond to the components of the differentials in Fig. 4b, and sp, th, sh, and sd stand for spring, thigh, shin, and step down, respectively, as depicted in Fig. 4. Throughout this paper, the notation for coordinates and torques in Table I is used.

TABLE I: Notation for MABEL's coordinates and torques. Subscripts L and R denote left leg and right leg, respectively.

| | |
|---|---|
| $q_{\mathrm{LS_{L,R}}}$ | leg shape rotation angle |
| $q_{\mathrm{mLS_{L,R}}}$ | motor leg shape rotation angle |
| $q_{\mathrm{LA_{L,R}}}$ | leg angle rotation angle |
| $q_{\mathrm{mLA_{L,R}}}$ | motor leg angle rotation angle |
| $q_{\mathrm{LA_{L,R}}}$ | leg angle rotation angle |
| $q_{\mathrm{mLA_{L,R}}}$ | motor leg angle rotation angle |
| $q_{\mathrm{Bsp_{L,R}}}$ | Bsp rotation angle |
| $\tau_{\mathrm{mLS_{L,R}}}$ | mLS motor torque |
| $\tau_{\mathrm{mLA_{L,R}}}$ | mLA motor torque |
| $\tau_{\mathrm{Bsp_{L,R}}}$ | Bsp torque |

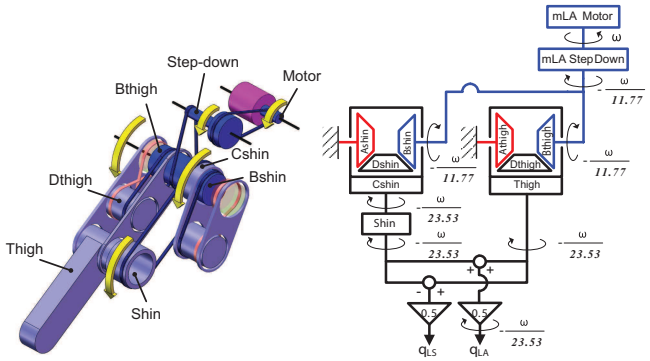


(a) $q_{\mathrm{LA}}$ pulley system (b) $q_{\mathrm{LA}}$ Transmission

Fig. 6: (a) Motor actuation is transmitted to $q_{\mathrm{LA}}$ through one step-down pulley and two differentials (Thigh and Shin). (b) Transmission flow of $q_{\mathrm{LA}}$. Gear ratios are indicated.

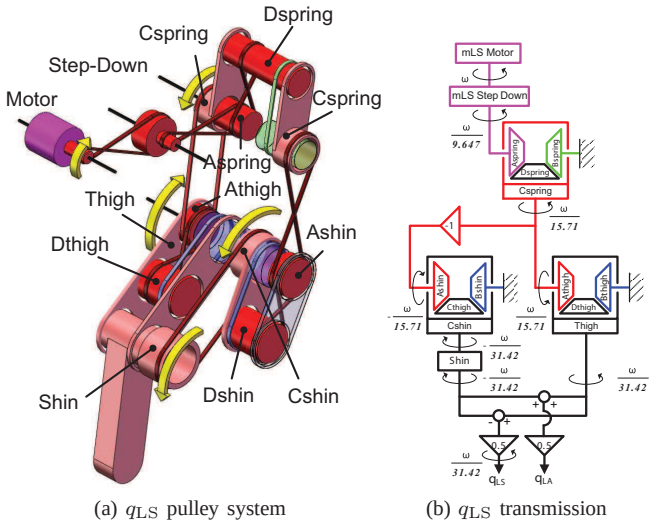


(a) $q_{\mathrm{LS}}$ pulley system (b) $q_{\mathrm{LS}}$ transmission

Fig. 7: (a) Motor actuation is transmitted to $q_{\mathrm{LS}}$ through one step-down pulley and three differentials (Spring, Thigh, and Shin). (b) Transmission flow of $q_{\mathrm{LS}}$. Gear ratios are indicated.

## III. Overview of System Identification Procedure

Current CAD packages provide excellent estimates of the total mass of links and pulleys, their lengths and radii, center of mass, and moments of inertia. If one also accounts for the location and mass of items not normally represented in a CAD drawing, such as bearing shape and density, cable length and density, electrical wiring, on-board power electronics, actuators and sensors, then good *a priori* estimates of total mass, center of mass and moments of inertia can be obtained for the overall robot. This was done for MABEL. Consequently, part of our system identification procedure is aimed at validating these *a priori* estimates by comparing predicted responses to experimental data.

In addition, there are important parameters for which reliable estimates are not available from the CAD drawings. These include motor torque constants, motor rotor inertias, and spring stiffness and pre-load. Even though motor torque constants and rotor inertias were provided by the manufacturer on the basis of their in-house CAD programs, the motors were custom wound with very small production numbers, and hence, these values were not experimentally verified before shipping. Moreover, because we have different motors for $\mathrm{mLA}$ and $\mathrm{mLS}$ actuation, and we also have different[2] $\mathrm{mLS}$ motors for left and right legs, the characteristics of these motors would be different in each case. The springs are custom built as well, and their stiffness must be identified. Finally, friction parameters will probably never be reliably estimated by a CAD program and must be determined experimentally.

### A. Steps in the Identification Process

The first phase of the experiments focuses on identifying the actuator parameters and the friction parameters in the transmission, as well as validating the pulley inertia estimates provided by the CAD program. The motor torque constant, $K_T$, and rotor inertia, $I_{rotor}$, of each motor are also determined. This is accomplished by analyzing a chain of rotating, symmetric inertias. Because the pulleys are connected by "rigid" (low stretching) steel cables to form a one-degree-of-freedom system, various paths in the transmission mechanism can be modeled simply by the lumped moment of inertia of the pulleys, and friction. This combined moment of inertia of the pulleys can be calculated by the CAD model and added to the rotor inertia of the motor. The corresponding lumped moment of inertia can be obtained also from experiments. From these data, motor torque constants, motor rotor inertias, viscous friction and motor torque biases can be estimated.

Next, the legs are included to validate the actuation-transmission model in conjunction with the center of mass and moments of inertias of the links constituting the thigh and shin. Each link's total mass, center of mass, and moment of inertia can be calculated accurately from the CAD model, so the primary objective of this step is to validate these values. For these experiments, the compliance is removed from the system by blocking the $B_{Spring}$ pulley; the torso is fixed as well.

[2]The use of motors of different characteristics for the left and right sides was not planned. It was a matter of necessity when one of the motors failed.

TABLE II: Parameters to be identified, where $\mathrm{i} \in \mathcal{I}$, $\ell \in \mathcal{L}$, and $\mathrm{t} \in \mathcal{T}$. Subscripts $\mathrm{L}$ and $\mathrm{R}$ denote left leg and right leg, respectively.

| | |
|---|---|
| Differentials and Motors | |
| $K_{\mathrm{i}}$ | motor torque constant |
| $J_{\mathrm{i}}^{rotor}$ | inertia of the rotor |
| $J_{\mathrm{t}}$ | inertia of the transmission pulleys |
| $\mu_{\mathrm{i}}$ | friction coefficient |
| $b_{\mathrm{i}}$ | motor bias |
| Thigh and Shin (Leg) | |
| $m_\ell$ | mass of the link $\ell$ |
| $J_\ell$ | inertia of the link $\ell$ |
| $m_\ell r_{x,\ell}$ | center of mass in x of the link $\ell$ multiplied by mass of the link $\ell$ |
| $m_\ell r_{y,\ell}$ | center of mass in y of the link $\ell$ multiplied by mass of the link $\ell$ |
| Compliance (Spring) | |
| $K_{B_{\mathrm{L,R}}}$ | spring stiffness |
| $Kd_{B_{\mathrm{L,R}}}$ | spring damping coefficient |
| $K_{C,\mathrm{i}}$ | cable stretch stiffness |
| $Kd_{C,\mathrm{i}}$ | cable stretch damping coefficient |

Following this experiment, the torso's inertial parameters are identified. Due to the difficulties in experimental identification of the torso explained in Section VI, we chose to extract the inertial parameters from the CAD model and verify some of them with static experiments. The compliance is determined last. MABEL has two kinds of compliance. One is the unilateral, fiberglass spring designed into the transmission. The other source of compliance is unplanned and arises from stretching of the cables between the pulleys. The compliance of the unilateral spring will be obtained from static experiments, and the compliance from cable stretch will be estimated from dynamic experiments.

With the parameters obtained above, we can construct an overall dynamic model of the robot. A dynamic hopping experiment will be executed and the results will be compared with simulation results of the dynamic model. The parameters to be identified are shown in Table II.

### B. Experimental Setup for Motor, Differential, and Leg Parameters

The first phase of the experiments uses the setup depicted in Fig. 8. The torso is fixed relative to the world frame and the legs can freely move. The position of the $B_{Spring}$ pulley is fixed as well, removing compliance from the picture for the initial identification phase. Desired torque commands are sent to the amplifiers and are recorded by the computer. In turn, the amplifiers regulate the currents in the motor windings, thereby setting motor torque values. Rotational motions of the motors are transmitted to the thigh and shin links through the transmission differentials as shown in Fig. 6, 7, and 8.

Encoders are placed on the $q_{\mathrm{LA}}$ and $q_{\mathrm{LS}}$ motor angles, the $C_{Thigh}$ and $D_{Thigh}$ pulleys, and the knee joint. The position of the $B_{Spring}$ pulley is also measured, but is not used here because this pulley is locked in a constant position to remove the compliance. With this configuration, the $q_{\mathrm{LA}}$ and $q_{\mathrm{LS}}$ motor angles are rigidly connected to the angles $q_{\mathrm{LA}}$ and $q_{\mathrm{LS}}$ which are related to the motor encoder readings by the

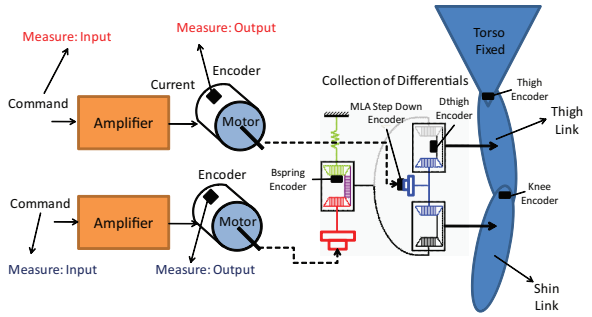


Fig. 8: Experimental setup for system identification. Motor commands are logged as an input for system identification and the encoder signals for motor angles, $C_{Thigh}$, $D_{Thigh}$ pulleys, and the knee joint are saved as outputs for system identification.

following relations:[3]

$$q_{\mathrm{LA}} = \frac{1}{\gamma_{\mathrm{LA}\to\mathrm{mLA}}} q_{\mathrm{mLA}}, \text{ and} \tag{5}$$

$$q_{\mathrm{LS}} = \frac{1}{\gamma_{\mathrm{LS}\to\mathrm{mLS}}} q_{\mathrm{mLS}} + \frac{1}{\gamma_{\mathrm{LS}\to\mathrm{Bsp}}} q_{\mathrm{Bsp}}, \tag{6}$$

where $\gamma_{\mathrm{LS}\to\mathrm{mLS}} = 31.42$, $\gamma_{\mathrm{LA}\to\mathrm{mLA}} = -23.53$, and $\gamma_{\mathrm{LS}\to\mathrm{Bsp}} = 5.18$ are the gear ratios from LS to mLS, from LA to mLA and from LS to Bsp. The calculated $q_{\mathrm{LS}}$ and $q_{\mathrm{LA}}$ angles are also logged during the experiments.

It is common for power amplifiers to exhibit a small bias in commanded current, which in turn causes a small bias in motor torque. Before beginning system identification, these biases were estimated and compensated for each motor following the procedure described in Appendix A.

## IV. Transmission Identification

Recall that the differentials in the transmission are realized by a series of cables and pulleys; see Figs. 6 and 7. For system identification, this is an advantage because we can easily select how many pulleys are actuated by disconnecting cables. For each pulley combination, the lumped moment of inertia can be easily obtained by standard calculations. It follows that if the electrical dynamics of the motor and power amplifiers are neglected, the lumped pulley system can be modeled as a first-order system

$$J_{lumped}\dot{\omega} + \mu_{lumped}\omega = u, \tag{7}$$

where $J_{lumped}$ is the lumped moment of inertia, $\mu_{lumped}$ is the lumped friction coefficient, $\omega$ is angular velocity of the motor, and $u$ is commanded motor torque. By identifying $J_{lumped}$ and $\mu_{lumped}$ for three different combinations of pulleys plus motor, it is possible to determine $K_T$ and $J^{rotor}$, and to validate the lumped pulley inertia predicted by the CAD model. In the following, for each side of the robot, the three pulley combinations of Fig. 9 will be used for the leg-angle path and the three pulley combinations of Fig. 10 will be used for the leg-shape path.

[3]These relations hold under the assumption that the cables do not stretch, which is a very good approximation here because relatively light loads are applied to the robot. In most of the robot's applications, however, such as walking and running, the transmission system is heavily loaded and significant cable stretching is observed. Models described in Section VII-B take into account cable stretch.

### A. Lumping the Pulley Inertias

In the following it is assumed that the position of the $B_{Spring}$ pulley is fixed and the cables do not stretch. The pulleys in the transmission are then rigidly connected and rotate with a gear ratio determined by the ratio of the radii of consecutive pulleys. Moreover, if the position of the leg-shape motor is constant, then the pulleys in the leg-angle path form a one-degree-of-freedom system as depicted in Fig. 11 and can therefore be lumped; a similar analysis holds when the position of the leg-angle motor is constant.

### B. Motor Torque Constant and Inertia Correction Factor

The $q_{\mathrm{LA}}$-identification experiments are performed successively on the $q_{\mathrm{LA}}$-motor in combination with 1, 3 and 5 pulleys as shown in Fig. 9. The $q_{\mathrm{LS}}$-identification experiments are performed successively on the $q_{\mathrm{LS}}$motor in combination with 1, 3, and 4 pulleys as shown in Fig. 10. The lumped moments of inertia of each combination, including the contributions of the cables can be expressed as

$$J_i = J^{rotor} + J_i^{pulley} + J_i^{cable}, \quad i = 1, 2, 3 \tag{8}$$

where $J^{rotor}$ is inertia of the actuator rotor, $i$ denotes experiment number, $J_i^{pulley}$ is the lumped pulley moment of inertia of experiment $i$ calculated from the CAD model with consideration of gear ratios between the pulleys, and $J_i^{cable}$ is the lumped cable moment of inertia calculated from mass of the cable per unit length and the length of the cable with consideration of gear ratios between the pulleys. Letting $J^{rotor,man}$ denote the nominal rotor inertia supplied by the manufacturer, we introduce a scale factor $\alpha$ via

$$\alpha = \frac{J^{rotor}}{J^{rotor,man}}, \tag{9}$$

which we seek to identify; see (11).

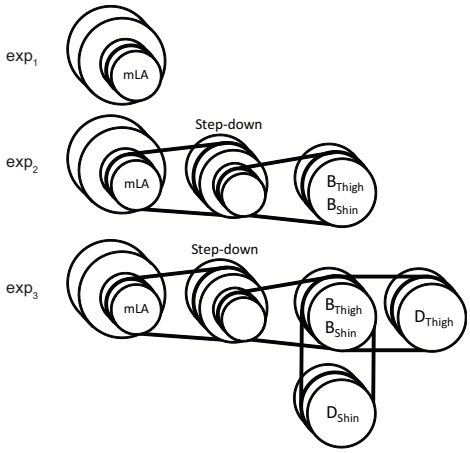


Fig. 9: Three different combinations for $q_{\mathrm{LA}}$ transmission identification.

Due to the presence of the amplifier, as shown in Fig. 12, the transfer function which can be experimentally estimated from commanded motor torque to measured motor angular velocity is a scalar multiple of (7). Hence, moment of inertia from the experiments is related to moment of inertia of (8) by,

$$J_i^{exp} = K_T(\alpha J^{rotor,man} + J_i^{pulley} + J_i^{cable}), \quad i = 1, 2, 3 \tag{10}$$

where $J_i^{exp}$ is lumped moment of inertia estimated on the basis of the $i$-th experiment.

Three different moment of inertia values, denoted by $J_1^{exp}$, $J_2^{exp}$, and $J_3^{exp}$ respectively, are obtained from each of the $q_{\mathrm{mLS}}$ and $q_{\mathrm{mLA}}$ experiments. Arranging the equations related with those inertias in matrix form gives

$$\Psi = \Gamma \begin{bmatrix} K_T\alpha \\ K_T \end{bmatrix} \tag{11}$$

where

$$\Psi = \begin{bmatrix} J_1^{exp} \\ J_2^{exp} \\ J_3^{exp} \end{bmatrix}, \text{ and } \Gamma = \begin{bmatrix} J^{rotor,man} & J_1^{pulley} + J_1^{cable} \\ J^{rotor,man} & J_2^{pulley} + J_2^{cable} \\ J^{rotor,man} & J_3^{pulley} + J_3^{cable} \end{bmatrix}.$$

$J_i^{exp}$ results from the experiments, $J^{rotor,man}$ is from the manufacturer's data sheet, and $J_i^{pulley}$ and $J_i^{cable}$ are from the CAD model. Estimated values of $K_T$ and $\alpha$ are then obtained by least squares fit:

$$\begin{bmatrix} K_T\alpha \\ K_T \end{bmatrix} = (\Gamma'\Gamma)^{-1}\Gamma'\Psi. \tag{12}$$

### C. Experimental Results

System inputs were designed as follows. Starting from a lower frequency of 0.5 Hz, the input frequency was increased in 17 steps to an upper frequency of 50 Hz. Each frequency was held constant for 10 periods until changing to the next faster frequency so that the system response would reach steady state. At each frequency increment, the magnitude was also incremented to keep the measured motor angular velocity from becoming too small. Fig. 13 displays examples of the input signal and corresponding system response. The Matlab System Identification Toolbox was used to identify the transfer function (7). TABLE III shows the results obtained from the experiments.

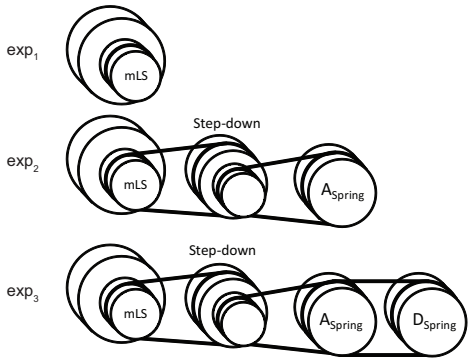


Fig. 10: Three different combinations for $q_{\mathrm{LS}}$ transmission identification.

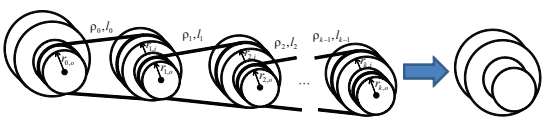

Fig. 11: A rigidly connected series of pulleys can be replaced with a single pulley representing the lumped moment of inertia.

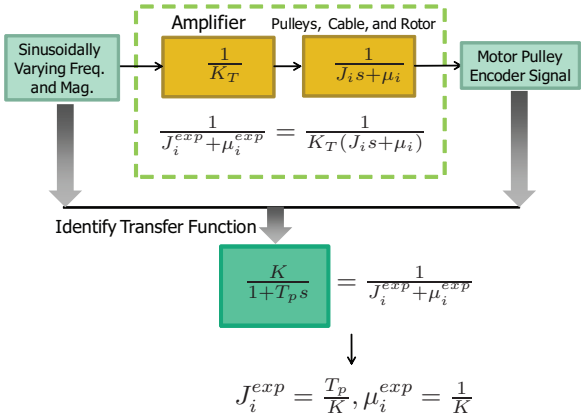


Fig. 12: Transfer function from input (amplifier command) to output (motor encoder signal). The motor torque constant and amplifier are lumped as a single parameter $K_T$. The measured transfer function is $1/(K_T(J_i s + \mu_i))$. The Matlab system identification toolbox is used to estimate the first-order transfer function from the experimental measurements.

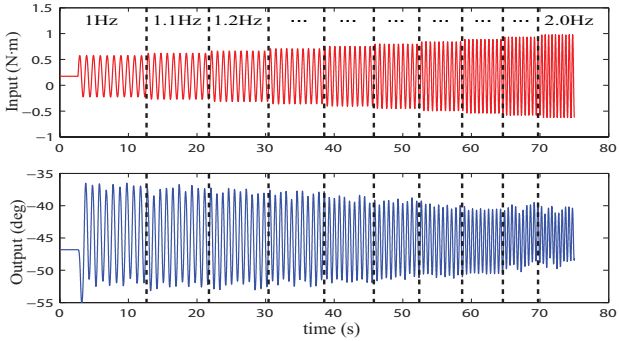


Fig. 13: Example of input and output for system identification. The input is a modified chirp signal, that is, a sinusoid with varying frequency and magnitude.

TABLE III: Identified experimental moments of inertia and friction coefficients for the transmission mechanism.

| | | $i$=1 | $i$=2 | $i$=3 |
|---|---|---|---|---|
| $\mathrm{mLS_L}$ | $J_i^{exp}$ (kg·m$^2$) | 8.819e-04 | 1.099e-03 | 1.112e-04 |
| | $\mu_i^{exp}$ (N·m·s) | 5.655e-03 | 6.518e-03 | 7.142e-03 |
| $\mathrm{mLA_L}$ | $J_i^{exp}$ (kg·m$^2$) | 5.514e-4 | 7.223e-4 | 7.436e-4 |
| | $\mu_i^{exp}$ (N·m·s) | 2.332e-03 | 4.365e-03 | 3.858e-03 |
| $\mathrm{mLS_R}$ | $J_i^{exp}$ (kg·m$^2$) | 1.104e-3 | 1.360e-3 | 1.431e-3 |
| | $\mu_i^{exp}$ (N·m·s) | 6.545e-03 | 9.811e-03 | 9.879e-03 |
| $\mathrm{mLA_R}$ | $J_i^{exp}$ (kg·m$^2$) | 5.217e-4 | 6.900e-4 | 7.328e-4 |
| | $\mu_{exp}$ (N·m·s) | 1.718e-03 | 4.048e-03 | 4.703e-03 |

On the basis of the values in Table III, $K_T$ and $\alpha$ were calculated by (12). Their estimated values are listed in TABLE IV, along with the motor bias. Note that the respective rotor inertia scale factors $\alpha$ for the left and right sides of the robot are very close in value. Also, the leg-angle motor torque constants $K_T$ are nearly identical for the left and right sides. For the leg-shape motors, the estimated motor torque constants $K_T$ are different; this is because the motor windings are different on the left and right sides, as noted in Section III. We also note that motor biases are very small compared with typical torques that one may see in walking experiments, which can easily exceed 2Nm for mLA and 8Nm for mLS [3].

TABLE IV: Identified $\alpha$, motor constant $K_T$ and motor bias $b$.

| | $\mathrm{i}=\mathrm{mLS_L}$ | $\mathrm{i}=\mathrm{mLA_L}$ | $\mathrm{i}=\mathrm{mLS_R}$ | $\mathrm{i}=\mathrm{mLA_R}$ |
|---|---|---|---|---|
| $\alpha_\mathrm{i}$ | 0.934 | 0.741 | 0.930 | 0.763 |
| $K_{T,\mathrm{i}}$ | 0.995 | 1.332 | 1.287 | 1.269 |
| $b_\mathrm{i}$(N·m) | -0.1076 | -0.04652 | 0.02995 | -0.001672 |

## V. Thigh and Shin Identification

This section focuses on the parameters associated with the legs. Thigh and shin identification are performed in two steps: SISO (Single Input Single Output) and MIMO (Multi Input Multi Output). In SISO identification, only one degree of freedom is actuated at a time: $q_{\mathrm{mLS_L}}$, $q_{\mathrm{mLA_L}}$, $q_{\mathrm{mLS_R}}$, or $q_{\mathrm{mLA_R}}$, and the other ones are mechanically locked. Because one degree of freedom is actuated, a reduced number of parameters appears in the dynamic model, so the system behavior is simple and easy to identify. Once parameters in the SISO dynamic model are identified, we proceed to MIMO experiments, where both $q_{\mathrm{mLS_L}}$ and $q_{\mathrm{mLA_L}}$ are actuated simultaneously or both $q_{\mathrm{mLS_R}}$ and $q_{\mathrm{mLA_R}}$ are actuated.

The main purpose of the MIMO experiments is to *validate* the parameters obtained in the SISO experiments. However, friction coefficients may differ from the values from Section IV because more joints are actuated when doing thigh and shin identification experiments than in the transmission identification experiments. Recall that Fig. 4b and 8 show how the thigh and shin links are actuated by the torque transmitted through the transmission.

In this section, the torso continues to be fixed relative to the world frame and the position of the $B_{Spring}$ pulley is fixed as well, removing compliance from the picture. The motor torque constants and rotor inertias identified in Section IV are used in the model.

### A. Mathematical Model

Because we assume rigid connections between $q_{\mathrm{LA}}$ and $q_{\mathrm{mLA}}$, and between $q_{\mathrm{LS}}$ and $q_{\mathrm{mLS}}$ in the leg identification, the appropriate set of generalized coordinates for the dynamics of the combined leg and transmission systems is $q_g = [q_{\mathrm{mLS_L}}, q_{\mathrm{mLA_L}}, q_{\mathrm{mLS_R}}, q_{\mathrm{mLA_R}}]$.

In the following, $\mathcal{Q} \subset \mathcal{I}$ in (2) represents coordinates of $\mathcal{I}$ that are actuated in a given experiment and will be called the actuated index set. Similarly, let $\mathcal{P} \subset \mathcal{I}$ be the complement of $\mathcal{Q}$; its elements correspond to the mechanically locked coordinates of $\mathcal{P}$, referred to as the locked index set. For example, suppose that only the $\mathrm{mLS_L}$ and $\mathrm{mLA_L}$ motor angles are actuated and the other coordinates are mechanically locked, then $\mathcal{Q} = \{\mathrm{mLS_L}, \mathrm{mLA_L}\}$ and $\mathcal{P} = \{\ \mathrm{mLS_R},\ \mathrm{mLA_R}\}$. We also define the set of coordinates $q_Q = \left[q_{\mathrm{q}_1}, \ldots, q_{\mathrm{q}_{\mathrm{n}_\mathcal{Q}}}\right]$, where $\mathrm{q}_1, \ldots, \mathrm{q}_{\mathrm{n}_\mathcal{Q}} \in \mathcal{Q}$, and $\mathrm{n}_\mathcal{Q}$ is the number of elements in the set $\mathcal{Q}$, and $q_\mathcal{P} = \left[q_{\mathrm{p}_1}, \ldots, q_{\mathrm{p}_{\mathrm{n}_\mathcal{P}}}\right]$, where $\mathrm{p}_1, \ldots, \mathrm{p}_{\mathrm{n}_\mathcal{P}} \in \mathcal{P}$, and $\mathrm{n}_\mathcal{P}$ is the number of elements in the set $\mathcal{P}$.

The parameters to be validated from the CAD model are grouped in a vector $\theta = [\mathbf{m} \quad \mathbf{I} \quad \mathbf{r_x} \quad \mathbf{r_y}]$, where $\mathbf{m}$, $\mathbf{I}$, $\mathbf{r_x}$ and $\mathbf{r_y}$ are mass, inertia, center of mass position in $x$, and in $y$, respectively (the values from the CAD model are presented in Appendix B), and let $\alpha = [\alpha_{\mathrm{mLS_L}},\ \alpha_{\mathrm{mLA_L}},\ \alpha_{\mathrm{mLS_R}},\ \alpha_{\mathrm{mLA_R}}]$ from Table IV. The total kinetic energy for the actuated index set $\mathcal{Q}$ is

$$\begin{aligned}\mathcal{K}_Q\left(q_g, \dot{q_g}\,\theta, \alpha\right) =& \mathcal{K}^{Thigh}\left(q_g, \dot{q_g}, \theta, \alpha\right)|_{q_P = q_P^*} \\ &+ \mathcal{K}^{Shin}\left(q_g, \dot{q_g}, \theta, \alpha\right)|_{q_P = q_P^*} \\ &+ \mathcal{K}^{trans}\left(q_g, \dot{q_g}, \theta, \alpha\right)|_{q_P = q_P^*}\end{aligned} \tag{13}$$

where, $\mathcal{K}^{Thigh}$, $\mathcal{K}^{Shin}$, and $\mathcal{K}^{trans}$ are the kinetic energies of the thigh, the shin and the transmission, respectively, and $q_P^*$ are the locked joint position angles for $q_P$. Symbolic expressions for the transmission model are available online at [25]. The total potential energy for the actuated index set $\mathcal{Q}$ is

$$\begin{aligned}\mathcal{V}_Q\left(q_g, \dot{q_g}\,\theta, \alpha\right) =& \mathcal{V}^{Thigh}\left(q_g, \dot{q_g}, \theta, \alpha\right)|_{q_P = q_P^*} \\ &+ \mathcal{V}^{Shin}\left(q_g, \dot{q_g}, \theta, \alpha\right)|_{q_P = q_P^*} \\ &+ \mathcal{V}^{Trans}\left(q_g, \dot{q_g}, \theta, \alpha\right)|_{q_P = q_P^*}.\end{aligned} \tag{14}$$

The Lagrangian is then

$$\mathcal{L}_Q = \mathcal{K}_Q - \mathcal{V}_Q. \tag{15}$$

With the total kinetic energy and potential energy obtained from (13) and (14), the dynamics can be determined through Lagrange's equations:

$$\frac{d}{dt}\frac{\partial \mathcal{L}_Q}{\partial \dot{q}_Q} - \frac{\partial \mathcal{L}_Q}{\partial q_Q} = \Gamma_Q, \tag{16}$$

where $\Gamma_Q$ is the vector of generalized forces acting on the robot, and can be written as:

$$\Gamma_Q = I_{\mathrm{n_q}\times\mathrm{n_q}} K_{T_Q} u_Q - F_\mu \dot{q}_Q, \tag{17}$$

where $I_{\mathrm{n_q}\times\mathrm{n_q}}$ is the identity matrix of size $\mathrm{n_q}$, $K_{T_Q} = diag[1/K_{T,\mathrm{q_1}} \cdots 1/K_{T,\mathrm{q_{n_p}}}]$, $u_Q = [\tau_{\mathrm{q_1}} + b_{\mathrm{q_1}} \cdots \tau_{\mathrm{q_{n_p}}} + b_{\mathrm{q_{n_p}}}]$, and $F_\mu = diag[\mu_{\mathrm{q_1}} \cdots \mu_{\mathrm{q_{n_p}}}]$, and where $K_{T,\mathrm{q_1 \cdots n_p}}$ are from Table IV. The $b_{\mathrm{q_1}}, \ldots, b_{\mathrm{q_{n_p}}}$ are the motor biases[4]. The motor biases can be obtained from Table IV for the SISO experiment; for the MIMO experiment, however, they are obtained as part of the optimization process explained in Section V-C. The friction coefficients are $\mu_{\mathrm{q_1}}, \ldots, \mu_{\mathrm{q_{n_p}}}$, and the procedure to obtain them will also be explained in Section V-C.

[4]Because the legs are relatively light, small torque biases lead to significant errors in the modeled effects of gravity. When the robot is in actual operation and supporting the heavy torso, the effects of these small torque biases will be negligible.

The dynamic model in (16) also can be written in the form

$$D(\theta,\alpha,q)\ddot{q} + C(\theta,\alpha,q,\dot{q})\dot{q} + G(\theta,\alpha,q) = \Gamma_Q, \qquad (18)$$

where $D(\theta,\alpha,q)$ is the inertia matrix, $C(\theta,\alpha,q,\dot{q})$ is the Coriolis matrix, $G(\theta,\alpha,q)$ is the gravity vector.

### B. Experiments

Two types of experiment are performed in this section: SISO and MIMO. Each is performed on one leg at a time. In principle, with the torso position fixed, the legs are decoupled; in practice, there is some coupling of vibration from one side to the other because the test stand is not perfectly rigid.

In the SISO experiments, one degree of freedom is actuated and logged (either $q_{\mathrm{mLS}}$ or $q_{\mathrm{mLA}}$), while the other degree of freedom is mechanically locked. In the MIMO experiment, both $q_{\mathrm{mLS}}$ and $q_{\mathrm{mLA}}$ are actuated and recorded. The objective of the SISO experiments is to validate the parameter vector $\theta$ in (18) obtained from the CAD model, and the motor constant $K_T$ and bias $b$ terms identified in Section IV. The objective of the MIMO experiment is to validate the parameters from the SISO experiment.

The input signal is a modified chirp signal plus a constant offset, similar to the transmission identification experiments. However, there is an additional complication: the magnitude and offset must be selected to keep the links within the robot's work space. Previously, when the transmission was disconnected from the legs, this was not an issue.

### C. Simulation and Validation

With all the parameters in the mathematical model (18) known, the response of the system excited by the input used in experiments can be simulated. The parameter $\theta$ in (18) can be obtained from the CAD model, and $\alpha$, $b$, and $K_T$ was obtained in Section IV. The friction parameters $\mu$ are obtained by minimizing the following cost function

$$J(\mu_{\mathcal{Q}}) = \sqrt{\sum(y_{exp} - y_{sim}(\mu_{\mathcal{Q}}))}, \qquad (19)$$

where $y_{exp}$ is the vector of experimentally measured data, $y_{sim}$ is the vector of simulated data, and $\mu_{\mathcal{Q}}$ is the vector of viscous friction coefficients given the actuated index set $\mathcal{Q}$. The $\mu_{\mathcal{Q}}$ values obtained in this manner should be larger than the values from Section IV, but not greatly different from those values, and are shown in Table V.

In the MIMO simulations, we observed that very small variations in assumed actuator bias, which can be ignored in nominal use of the robot, can cause large deviations in the system response, especially in the leg-shape variables $q_{\mathrm{mLS}}$. Therefore, for the MIMO simulations, in place of the bias values obtained from the transmission identification, we used values which minimize the cost function,

$$J(b_{\mathcal{Q}}) = \sqrt{\sum(y_{exp} - y_{sim}(b_{\mathcal{Q}}))}, \qquad (20)$$

where $y_{exp}$ is the vector of experimentally measured data, $y_{sim}$ is the vector of simulated data, and $b_{\mathcal{Q}}$ is the bias vector of the actuated index set $\mathcal{Q}$. The values obtained for $b_{\mathcal{Q}}$ are shown in Table V.

TABLE V: Friction coefficient $\mu$ and motor bias $b$ obtained by minimizing the costs in (19) and (20), respectively.

| | $\mathrm{i} = \mathrm{mLS_L}$ | $\mathrm{i} = \mathrm{mLA_L}$ | $\mathrm{i} = \mathrm{mLS_R}$ | $\mathrm{i} = \mathrm{mLA_R}$ |
|---|---|---|---|---|
| $\mu_{\mathrm{i}}$ (N·m·s) | 9.844e-3 | 4.316e-3 | 9.027e-3 | 4.615e-3 |
| $b_{\mathrm{i}}$ (N·m) | -8.417e-3 | 2.597e-2 | -1.446e-2 | -2.461e-3 |

Simulations are conducted as follows. First, (18) is set up for a given actuated index set $\mathcal{Q}$. Then, the system response is simulated for the input sequence used in the experiment. Finally, the results from simulation are compared with experiments. The overall simulation and validation procedures are depicted in Fig. 14.

### D. Results

The comparisons between simulated and experimental results are presented in Fig. 15 and Fig. 16[5]. All figures show $q_{\mathrm{LS}}$ and $q_{\mathrm{LA}}$ computed from $q_{\mathrm{mLS}}$ and $q_{\mathrm{mLA}}$ because $q_{\mathrm{LS}}$ and $q_{\mathrm{LA}}$ are physically more meaningful and easier to understand. It is emphasized that all parameters are either from the transmission identification experiments or the CAD model, with the following exceptions: friction is estimated in the SISO experiments from (19) and used in the MIMO experiments; in the MIMO experiments, motor biases are tuned via (20).

We can observe that simulation results match very closely the experimental results. The small differences in the plots may arise from several sources:

1) A simple viscous friction model is used in the simulations. This model does not take into account stick-slip behavior in the slow velocity region.
2) Electrical wiring is not included in calculating inertial parameters.
3) Motor bias changes slightly for each experimental trial.

## VI. Torso Identification

Due to the torso being much heavier than the legs, its mass and inertia strongly affect the dynamics of the robot. Accurate identification of the torso's inertial parameter is therefore very important. The identification of the torso's inertial properties through experimentation is more difficult than those of the

[5]MATLAB .fig-files are available online at [25]

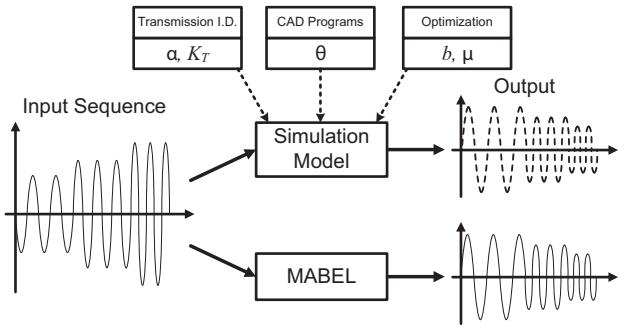


Fig. 14: Simtulaion and validation procedures of leg identificaion

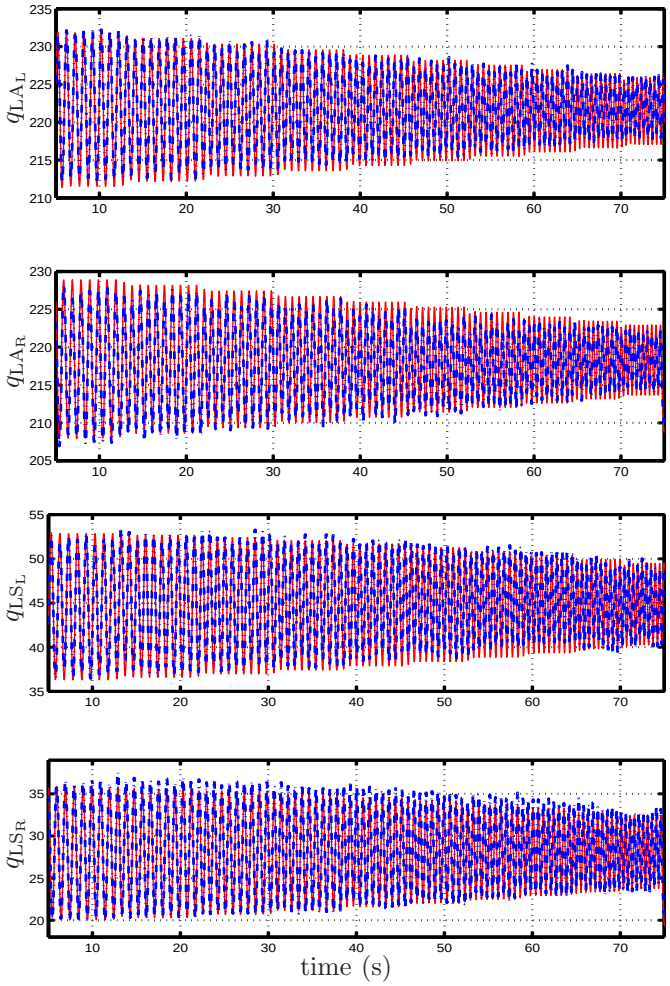


Fig. 15: SISO simulation (solid red line) and experimental (dotted blue line) data in degrees.

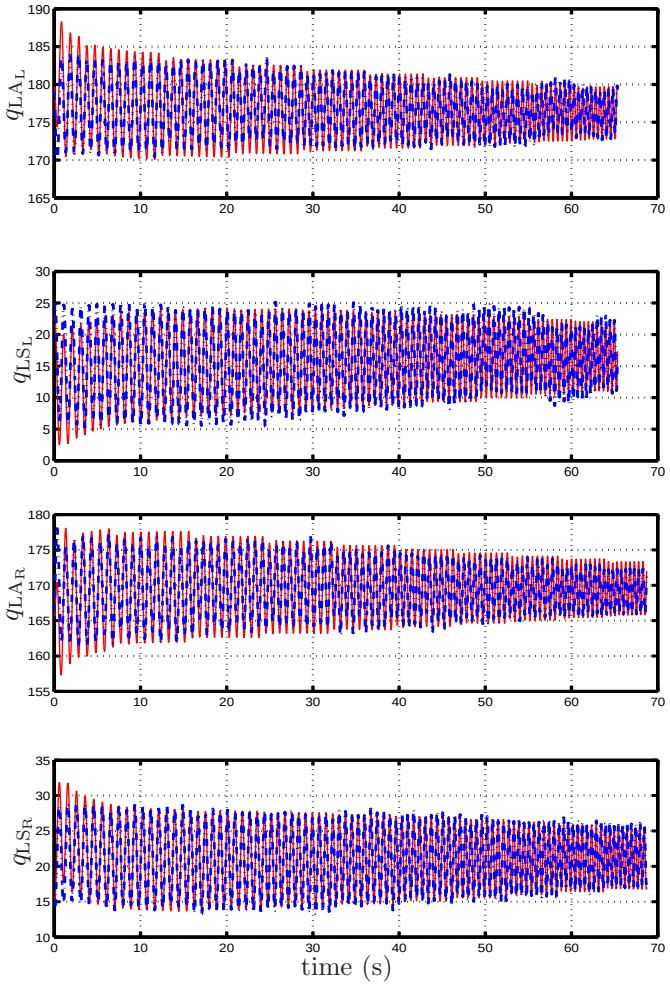


Fig. 16: MIMO simulation (solid red line) and experimental (dotted blue line) data in degrees.

transmission and legs for the following reasons. First, the experimental testbed does not allow[6] us to fix the legs and move only the torso. Second, the workspace of the torso is limited[7] to $+30^\circ \sim -40^\circ$.

Therefore, instead of dynamic identification of the torso, static balancing experiments are executed for validating *a priori* CAD model estimates. First, we set the robot in a posture where the right leg is extended more than the left leg. MABEL is then balanced by hand[8] on the right leg[9]. Once the robot is in balanced posture, the joint position data is recorded. Many different postures are balanced and logged. With the logged data, we calculate the center of mass position of the overall robot, and verify that the calculated center of mass is located over the supporting toe.

In a second set of experiments, the position of the hip joint is fixed, with the legs hanging below the robot and above the floor. The torso is balanced in the upright position. We then calculate the center of mass position of the model without the boom, and check that the center of mass is aligned over the hip joint.

We tried 10 different postures for the first experiment and 7 different postures for the second experiment. Fig. 17a displays the horizontal distance between the center of mass and the supporting toe for the first experiment, and Fig. 17b shows the horizontal distance between the center of mass and the hip for the second experiment. We observe that the maximum error is 6 mm, which is negligible considering that we did the experiments with manual balancing.

## VII. Compliance

MABEL uses springs connected in series between $q_{\mathrm{mLS}}$ and $q_{\mathrm{LS}}$ to provide energy storage and shock absorption. The stiffness of these springs is estimated through static experiments using the calculated spring torques and measured spring deflections. The joint torques used in these experiments are more representative of the torques used in walking [3] and are approximately 8 times higher than in the dynamic

[6]Attempts at doing so resulted in movements of the heavy torso (approximately 40 kg) being translated to the legs.

[7]The is due to a rotation limiter device installed to prevent the torso from hitting the floor when the robot falls. A related video is available on YouTube.

[8]The balance of the robot is maintained with very minimal fingertip pressure.

[9]The wheel at the toe is removed for better accuracy of the experiment. Due to compliance of the wheel and its rounded shape, the contact point would vary for each posture.

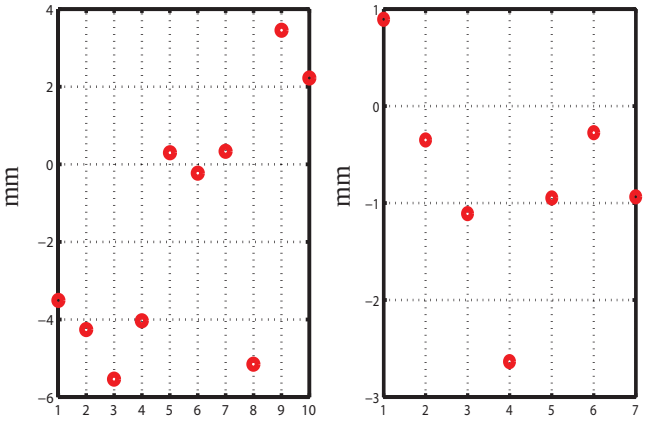


Fig. 17: Calculated center of mass horizontal distance from the supporting toe (a) and the hip (b) from the identified leg inertial parameters and the torso inertial parameters from the CAD models. All center of mass horizontal distances stay within 6mm.

experiments of Section V. During the experiments, it is noted that the cables in the differentials stretch. This compliance is also modeled.

### A. Spring Stiffness

The series compliance in the drivetrain is now identified by static, constant torque experiments, performed by balancing the robot on one leg at a time. The setup is illustrated in Fig. 18. In these experiments, the torso is no longer locked in place relative to the world frame (it is free). The actuators on one side of the robot are disabled; the leg on that side is folded and tied to the torso. On the other side, a PD-controller is used to maintain the leg angle at $180°$. A second PD-controller is used to set the nominal leg shape, which is varied from $10°$ to $30°$. An experimenter balances the robot in place with the toe resting on a scale placed on the floor; the experimenter adjusts the angle of the robot so that it is exactly balanced on the toe, as in Section VI.

In this position, the scale is measuring the combined weight of the robot and the boom. At steady state, the torque at the $C_{Spring}$ pulley is exactly balanced by sum of the torques at the $A_{Spring}$ and $B_{Spring}$ pulleys, by the design of the differential. The torque at the $C_{Spring}$ (denoted by $\tau_{gravity}$ in Fig. 18) is the weight of the robot transmitted through the thigh and shin differentials, and its magnitude is given by:

$$|\tau_{gravity}| = \left| \frac{1}{2} W_{robot} sin(q_{\mathrm{LS}}) \right|, \tag{21}$$

where $W_{robot}$ is the weight of the robot measured by the scale at the bottom of the foot. The absolute value is used because spring stiffness is positive. The torque at $A_{Spring}$ (denoted by $\tau_{Asp}$ in Fig. 18) is from the $q_{\mathrm{mLS}}$ motor reflected through the stepdown pulley, and the torque at the $B_{Spring}$ pulley (denoted by $\tau_{\mathrm{Bsp}}$ in Fig. 18) is due to the deflection of the spring and is given by:

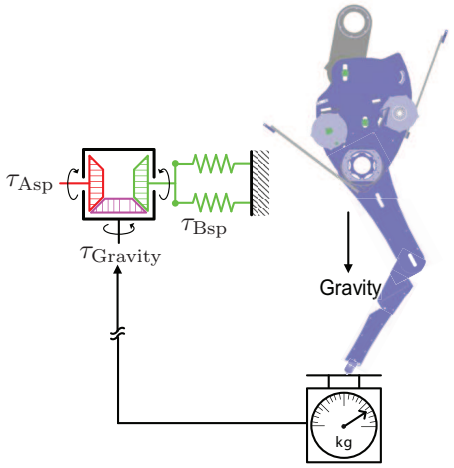


Fig. 18: Experimental setup for measuring spring stiffness. $C_{Spring}$ is locked in place by blocking the toe of the robot. Therefore, leg-shape motor torque is transmitted to the spring, resulting in spring defelction.

$$\tau_{\mathrm{Bsp}} = K_B q_{\mathrm{Bsp}}, \tag{22}$$

where $K_B$ is the spring stiffness and $q_{\mathrm{Bsp}}$ is the spring deflection measured by a magnetic encoder installed in the $B_{sp}$ pulley. Because $\tau_{Gravity}$ and $\tau_{\mathrm{Bsp}}$ are related via the differential mechanism, these torques are related by:

$$|\tau_{Gravity}| = |2.59061 \tau_{\mathrm{Bsp}}| . \tag{23}$$

Combining (21), (22), and (23), the spring stiffness is obtained as follows

$$K_B = \left| \frac{1}{5.18043} \frac{W_{robot} sin(q_{\mathrm{LS}})}{q_{\mathrm{Bsp}}} \right| . \tag{24}$$

We emphasize that the estimate in (24) does not depend on the estimated leg-shape motor torque. The design of the experiment is completed by varying $q_{\mathrm{LS}}$ over a range of values, here taken to be from $10°$ to $30°$.

The above experiment was performed on each leg. Fig. 19 shows the results of these experiments. It is observed that the spring behavior is nearly linear, and that the spring constants of the left and right springs are consistent.

### B. Cable Stretch

We have observed in walking experiments reported elsewhere [3] that the cables used in the differentials stretch a noticeable amount under the application of heavy loads[10]. This compliance breaks the rigid relations in (5) and (6). Consequently, $q_{\mathrm{LA}}$ and $q_{\mathrm{mLA}}$ are independent degrees of freedom, as are $q_{\mathrm{LS}}$, $q_{\mathrm{mLS}}$, and $q_{\mathrm{Bsp}}$.

We take into account the stretching of the cables with a simple spring model. First, the rigid relations are expressed in the form of a constraint

$$\lambda(q) = \begin{bmatrix} q_{\mathrm{mLA}} + \gamma_{\mathrm{LA}\to\mathrm{mLA}} q_{\mathrm{LA}} \\ q_{\mathrm{mLS}} - \gamma_{\mathrm{LS}\to\mathrm{mLS}} q_{\mathrm{LS}} - \gamma_{\mathrm{LS}\to\mathrm{Bsp}} q_{\mathrm{Bsp}} \end{bmatrix}, \tag{25}$$

[10]For the experiments reported in Sections V, the amount of cable stretch was negligible.

where $q$ is the vector of generalized coordinates for the robot dynamics and $\lambda(q) \equiv 0$ corresponds to zero cable stretch. Because the cable stretch torques act on these constraints, the corresponding input matrix for cable stretch forces $B_{cable}$ follows from the principle of virtual work:

$$B_{cable} = \frac{\partial \lambda}{\partial q}^{'}. \tag{26}$$

We assume here that the cable stretch torques can be modeled as a linear spring with linear damping. Therefore, for each of the four actuators, the spring force from the cable stretch is modeled as

$$\tau_{cable}(q, \dot{q}) = K_C \lambda(q) + K d_C \lambda(\dot{q}), \tag{27}$$

where $K_C$ is $2 \times 2$ a diagonal matrix spring coefficients, and $Kd_C$ is $2 \times 2$ diagonal matrix with damping coefficients of the cable stretch.

The spring and damping coefficients of the cables will be obtained in Section VIII-C.

## VIII. Overall Model Evaluation via Two-Legged Hopping

This section describes a hopping experiment used to fine tune and subsequently validate the overall dynamic model of MABEL. First, a dynamic model appropriate for two-legged hopping is presented. The model consists of the integration of the models for the transmission, the legs, the torso, and the cable stretch from Section IV, Section V, Section VI and Section VII-B, respectively, with a model to compute ground reaction forces [26], [27]. Next, a simple controller to induce two-legged hopping is summarized, with details given in Appendix C. With the simple controller, several hopping steps were realized, but a stable, steady-state hopping gait was not achieved. This data was used to determine the remaining parameters in the overall dynamic model, corresponding to the damper which implements the hard stop in the unilateral spring, the coefficients of the cable stretch model, and the ground contact model. Using this final model, the hopping controller was refined with event-based correction terms. When applied to the robot, this controller yielded successful hopping, which was terminated after 92 hops. The results of the hopping experiment are used to validate the model through comparison with the simulation model. Excellent agreement is attained.

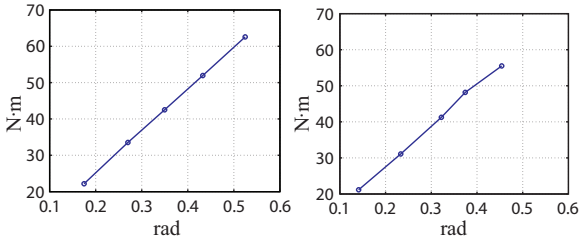


(a) Left Spring (b) Right Spring

Fig. 19: (a) Spring Stiffness=115.1N·m ($\tau_{\mathrm{Bsp_L}} = 115.1 q_{\mathrm{Bsp_L}} + 2.214$) (b) Spring Stiffness=111.7N·m ($\tau_{\mathrm{Bsp_L}} = 111.7 q_{\mathrm{Bsp_L}} + 5.377$)

### A. Dynamic Model

The model for the dynamic hopping is derived with the method of Lagrange. When deriving the equations of motion, it is more convenient to consider the spring torques, the cable stretch torques, the ground reaction forces and the joint friction torques as external inputs to the model. The Lagrangian is computed as summarized in [3], except that, because of the additional cable stretch dynamics, 4 additional coordinates are needed to parametrize the robot's linkage and transmission.

The generalized coordinates are taken as $q_{\mathrm{h}} := (q^L_{\mathrm{LA}}; q^L_{\mathrm{mLA}}; q^L_{\mathrm{LS}}; q^L_{\mathrm{mLS}}; q^L_{\mathrm{Bsp}}; q^R_{\mathrm{LA}}; q^R_{\mathrm{mLA}}; q^R_{\mathrm{LS}}; q^R_{\mathrm{mLS}}; q^R_{\mathrm{Bsp}}; q_{\mathrm{Tor}}; p^h_{\mathrm{hip}}; p^v_{\mathrm{hip}})$, where as in Fig. 2, and Fig. 4b, $q_{\mathrm{Tor}}$ is the torso angle, and $q_{\mathrm{LA}}$, $q_{\mathrm{mLA}}$, $q_{\mathrm{LS}}$, and $q_{\mathrm{mLS}}$ are the leg angle, leg-angle motor position, the leg shape, the leg-shape motor position respectively, and $p^h_{\mathrm{hip}}$ and $p^v_{\mathrm{hip}}$ are the horizontal and vertical positions of the hip in the sagittal plane, respectively. The model is then expressed in standard form as

$$D_{\mathrm{h}}(q_{\mathrm{h}}) \ddot{q}_{\mathrm{h}} + C_{\mathrm{h}}(q_{\mathrm{h}}, \dot{q}_{\mathrm{h}}) \dot{q}_{\mathrm{h}} + G_{\mathrm{h}}(q_{\mathrm{h}}) = \Gamma_{\mathrm{h}} \tag{28}$$

where, $\Gamma_{\mathrm{h}}$ is the vector of generalized forces and torques acting on the robot, which is given by,

$$\Gamma_{\mathrm{h}} = B_{\mathrm{h}} u + B_{fric} \tau_{fric}(q_{\mathrm{h}}, \dot{q}_{\mathrm{h}}) + B_{sp} \tau_{\mathrm{Bsp}}(q_{\mathrm{h}}, \dot{q}_{\mathrm{h}}) + \frac{\partial f}{\partial q_{\mathrm{h}}}^{'} F + B_{cable} \tau_{cable}(q_{\mathrm{h}}, \dot{q}_{\mathrm{h}}). \tag{29}$$

Here, $f$ is the position vector of the leg end, $F$ is the ground reaction force, the matrices $B_{\mathrm{h}}$, $B_{fric}$, $B_{\mathrm{Bsp}}$, and $B_{cable}$ are derived from the principle of virtual work and define how the actuator torques $\tau$, the joint friction forces $\tau_{fric}$, the spring torques $\tau_{\mathrm{Bsp}}$, and the cable stretch torques $\tau_{cable}$ enter the model, respectively.

The ground reaction forces at the leg ends are based on the compliant ground model in [26], [27], using the modifications proposed in [28]. The model for the unilateral spring is augmented with terms to represent the hard stop, yielding $\tau_{\mathrm{Bsp}}$ :

$$\begin{cases} = -K_B q_{\mathrm{Bsp}} - K d_B \dot{q}_{\mathrm{Bsp}}, & q_{\mathrm{Bsp}} > 0 \\ = -K_B q_{\mathrm{Bsp}} - K_{d1} q^3_{\mathrm{Bsp}} - K_{vd1} \dot{q}_{\mathrm{Bsp}}, & q_{\mathrm{Bsp}} \leq 0 \text{ and } \dot{q}_{\mathrm{Bsp}} \geq 0 \\ = -K_B q_{\mathrm{Bsp}} - K_{d1} q^3_{\mathrm{Bsp}} - K_{vd1} \dot{q}_{\mathrm{Bsp}} & \\ \quad - K_{vd2} \sqrt{|\dot{q}_{\mathrm{Bsp}}|} sign(\dot{q}_{\mathrm{Bsp}}), & q_{\mathrm{Bsp}} \leq 0 \text{ and } \dot{q}_{\mathrm{Bsp}} < 0 \end{cases} \tag{30}$$

where $K_B$ corresponds to the experimental values in Fig. 19, and where the remaining parameters $Kd_B$,$K_{d1}$,$K_{vd1}$, and $K_{vd2}$ will be identified from hopping data in Section VIII-C. When the spring is deflected, $q_{\mathrm{Bsp}} > 0$, this model is a linear spring damper. When $q_{\mathrm{Bsp}} \leq 0$, the pulley is against the hard stop, a very stiff damper. This model captures the unilateral nature of MABEL's built-in compliance.

### B. Hopping Controller

A simple, heuristic controller is outlined for hopping. It is emphasized that we are not interested in hopping per se. A hopping gait is being used as a means of exciting all the dynamic modes that will be present when running on flat ground or walking on uneven ground. The details of the controller are provided in Appendix C.

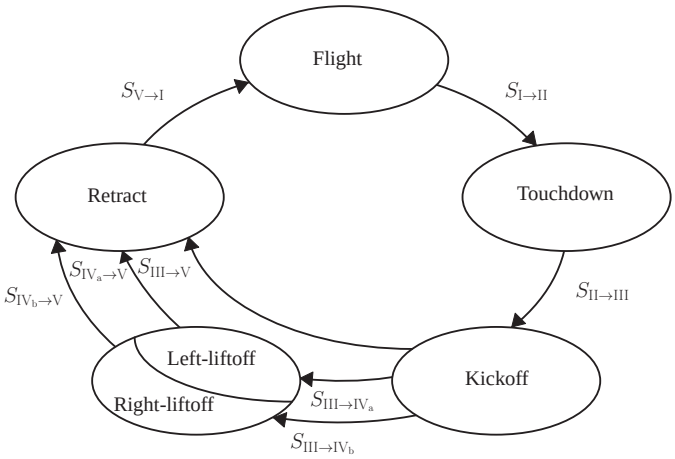


Fig. 20: The controller phases and the transitions. From Phase III, three possible transitions can occur because which leg comes off ground first cannot be predicted. According to which leg comes off the ground, controller selects Phase $\mathrm{IV_a}$,$\mathrm{IV_b}$ or; V as the next phase

The controller consists of 5 different phases as depicted in Fig. 20:

1) Phase I (Flight Phase): MABEL is in the air, and no ground contact occurs. The variables $q_{\mathrm{LA_L}}$, $q_{\mathrm{mLS_L}}$, $q_{\mathrm{LA_R}}$, and $q_{\mathrm{mLS_R}}$ are commanded to constant values via a PD controller.
2) Phase II (Touchdown Phase): MABEL lands on the ground[11]. The leg-angle motors are used to regulate the torso angle and the angle between left and right legs to constant values $h^d_{\mathrm{Tor}}$ and $\delta_{\mathrm{LA}}$, respectively. The leg-shape motor positions $q_{\mathrm{mLS_L}}$ and $q_{\mathrm{mLS_R}}$ are commanded to be constant so that the springs absorb the impact energy.
3) Phase III (Kickoff Phase): When the horizontal component of the center of mass velocity approaches zero, the legs are extend by $\delta^-_{\mathrm{LS_L}}$ for the left and $\delta^-_{\mathrm{LS_R}}$ for the right in order to propel the robot off the ground. From Phase III, three possible transitions can occur because which leg comes off the ground first cannot be predicted. According to which leg comes off the ground first, controller chooses Phase $\mathrm{IV_a}$, $\mathrm{IV_b}$ or ,V as the next phase.
4) Phase $\mathrm{IV_a}$ (Left-liftoff Phase): Only the left leg has lifted off the ground, and the right leg is still in contact with the ground. The left leg starts to retract by $\delta^+_{\mathrm{LS_L}}$ to provide clearance.
5) Phase $\mathrm{IV_b}$ (Right-liftoff Phase): Only the right leg has lifted off the ground, and the left leg is still in contact with the ground. The right leg starts to retract by $\delta^+_{\mathrm{LS_R}}$ to provide clearance.
6) Phase V (Retract Phase): Both legs have lifted off the ground, and are retracted for 50 msec to provide clearance. After 50 msec, the controller passes to the flight phase.

[11]Landing is declared when both legs touch the ground.

TABLE VI: Parameters obtained from dynamic hopping experiment.

| Spring Model | | | |
|---|---|---|---|
| $Kd_B$ | 1.5 | $K_{vd1}$ | 1000 |
| $K_{d1}$ | 100 | $K_{vd2}$ | 50 |

| Cable Stretch Model | | | | |
|---|---|---|---|---|
| | $\mathrm{i}=\mathrm{mLS_L}$ | $\mathrm{i}=\mathrm{mLA_L}$ | $\mathrm{i}=\mathrm{mLS_R}$ | $\mathrm{i}=\mathrm{mLA_R}$ |
| $K_{C,\mathrm{i}}$ | 2.9565 | 3.5000 | 2.9565 | 3.8094 |
| $Kd_{C,\mathrm{i}}$ | 0.0402 | 0.0889 | 0.0804 | 0.3556 |

| Ground Model | | | |
|---|---|---|---|
| $\lambda^a_v$ | 3.0e6 | $\sigma_{h0}$ | 260.0 |
| $\lambda^b_v$ | 4.5e6 | $\sigma_{h1}$ | 2.25 |
| $n$ | 1.5 | $\alpha_{h0}$ | 1.71 |
| $k$ | 4.38e7 | $\alpha_{h2}$ | 0.54 |
| | | $\alpha_{h3}$ | 0.9 |

### *C. Identification of Parameters for Cable Stretch, Hard Stop (Damper), and the Ground Model*

The controller outlined in Section VIII-B was tuned on an approximate simulation model that assumed the cables are rigid. The controller was coded in C++ and implemented with a 1 ms sample time. When applied on MABEL, steady-state (stable) hopping was not achieved, with five hops being typical before the robot fell. This experimental result was used to tune the parameters in the hard stop model, the cable stretch model, and the compliant ground contact model, using a combination of hand adjustment and nonlinear least squares fitting. The resulting parameters are given in TABLE VI.

### *D. Hopping Experiments for Validation*

Using the parameters of TABLE VI, the stability of the nominal hopping controller was evaluated on the simulation model using a Poincaré map, and was found to be unstable. Event-based updates to the torso angle were added to achieve stability [4, Ch.4]; see Appendix C. The controller was then applied to MABEL, resulting in 92 hops before the test was deliberately terminated. Fig. 21 and 22 compare typical experimental results against the simulation results for the 31st and 32nd of the 92 hops. Fig. 21 depicts joint position angle. The experimental and simulation data match well; it can be observed that the period of the experimental data is longer than that of the simulation results by approximately 30 ms. Fig. 21 depicts joint torques. The simulation accurately predicts joint torques observed in the experiment. Fig. 23 depicts cable stretch in the motor coordinates. A significant amount of cable stretch is observed, with the model capturing it quite well.

## IX. Conclusions

System identification of a 5-link bipedal robot with a compliant transmission has been investigated. For each side of the robot, the transmission is composed of three cable differentials that connect two motors to the hip and knee joints in such a way that one motor controls the angle of the virtual leg consisting of the line connecting the hip to the toe, and the second motor is connected - in series with a spring - in order to control the length of the virtual leg. The springs serve both to isolate the reflected rotor inertia of the leg-shape motors from

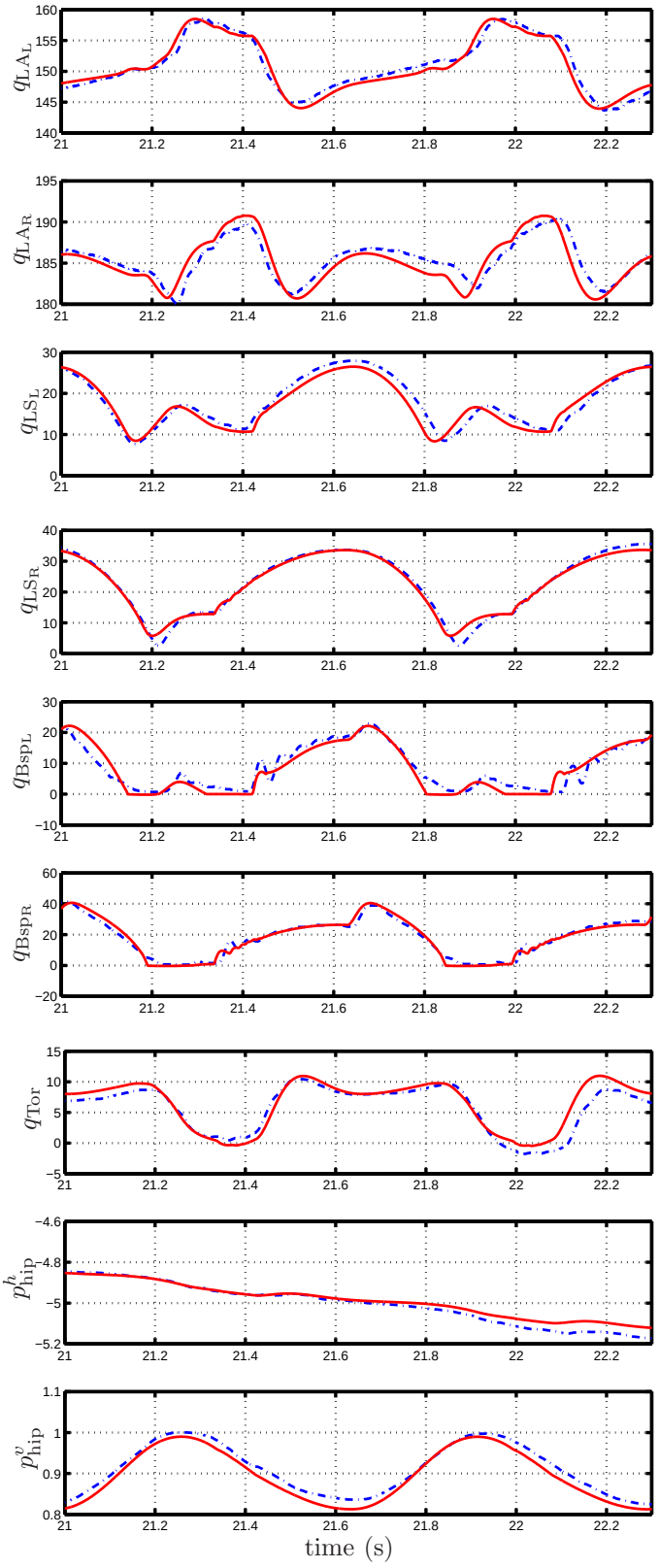


Fig. 21: Validation data from the second hopping experiment. Joint position (in degrees) and hip position (in m): simulation (solid red line) and experiment (dotted blue line).

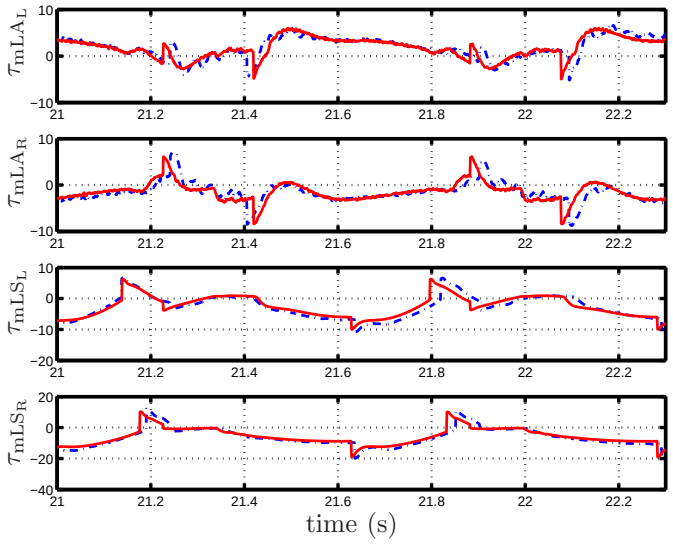


Fig. 22: Validation data from the second hopping experiment. Joint Torque (in N·m): simulation (solid red line) and experiment (dotted blue line).

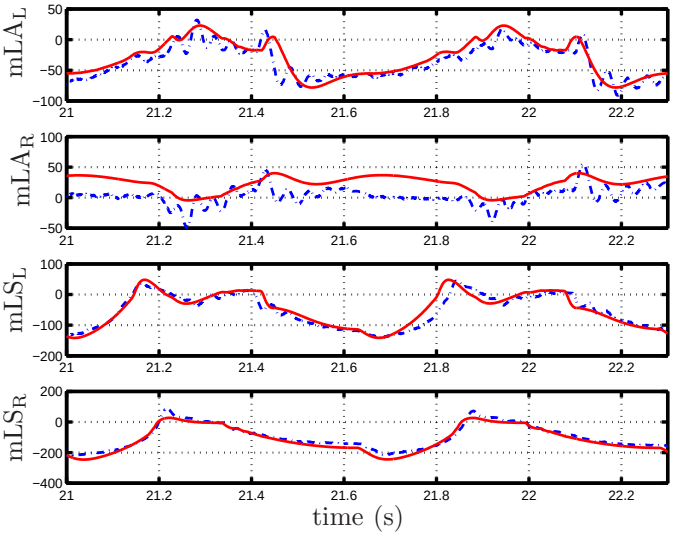


Fig. 23: Validation data from the second hopping experiment. Cable stretch (in degrees): simulation (solid red line) and experiment (dotted blue line).

the impact forces at leg touchdown and to subsequently store energy when the support leg must decelerate the downward motion of the robot's center of mass.

The robot is equipped with fourteen encoders to measure motor, pulley and joint angles, as well as contact switches at the ends of the legs. Neither force sensors, torque sensors, nor accelerometers are available. To get around these limitations, the identification procedure took full advantage of the modular nature of the robot. By selectively disconnecting cables in the transmission, various elements could be isolated for study. The process began by identifying the actuator parameters (rotor inertia and torque constants) and the viscous friction in the transmission, as well as validating the pulley inertia estimates provided by the CAD model, all with the cables removed

that connect the legs of the robot to the transmission. Next, the legs were included to validate the actuation-transmission model in conjunction with the center of mass and moments of inertias of the links comprising the thigh and shin. Each link's total mass, center of mass, and moment of inertia was estimated from the CAD model, so the primary objective of this step was to validate these values along with the identified actuator parameters. For these experiments, the compliance was removed from the system by blocking the appropriate pulley; the torso was rigidly fixed in an upright position as well. Following this, the mechanical parameters of the robot's torso were partially validated through static balancing experiments.

The compliance was identified last. MABEL has two kinds of compliance. One is the unilateral, fiberglass spring designed into the transmission. The other source of compliance is unplanned and arises from stretching of the cables between the pulleys. The compliance of the unilateral spring was obtained through static loading experiments. The compliance from cable stretch was estimated from a set of hopping experiments. From the same data set, the parameters for a compliant ground model were roughly estimated.

A complete dynamic model of the robot was constructed using the parameters identified in the above process. Using this model, a hopping controller was designed and simulated. When implemented on the robot, the controller yielded stable, steady hopping. After 92 hops, the experiment was terminated. A comparison of the experimental data and the model showed very good agreement. We are confident that this dynamic model will allow us to design and successfully implement controllers for running on a smooth floor and robust walking on an uneven floor.

## Appendix A
## Motor Bias

The motor amplifier bias is estimated by the following procedure. First, the motor pulley is isolated from all other pulleys by simply disconnecting the cable between the motor and the rest of the transmission, in order to minimize the effect of friction from the rest of the pulleys. The motor is actuated with an unbiased sinusoidal torque command. An unknown amplifier bias will causes the motor position to drift slowly as shown in Fig. 24. Differentiating the response of the motor shown in Fig. 24 gives the angular velocity, which is shown in Fig. 25. A first order ARX (Autoregressive model with exogenous inputs [29]) model is used to identify the system, because the transfer function between the input and the angular velocity can be modeled as a simple first order system (as explained in Section II). To identify the bias, a constant sequence of 1's is augmented to the original input signal as shown in Fig. 26. Thus, the input sequence used in estimating the bias is defined by,

$$u = \begin{bmatrix} u_{1,1}, \ldots, u_{1,k} \\ u_{2,1}, \ldots, u_{2,k} \end{bmatrix} = \begin{bmatrix} \tau \\ 1, \ldots, 1 \end{bmatrix}, \qquad (31)$$

where, $\tau$ is the original input sequence.

The first order ARX model with two inputs is given by,

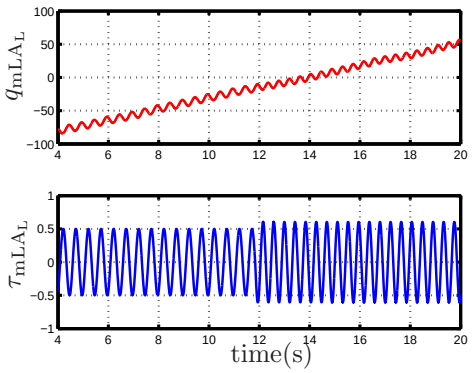


Fig. 24: The amplifier has an unknown bias. This is evident from the fact that an unbiased command input to the amplifier, produces an output which slowly drifts with time.

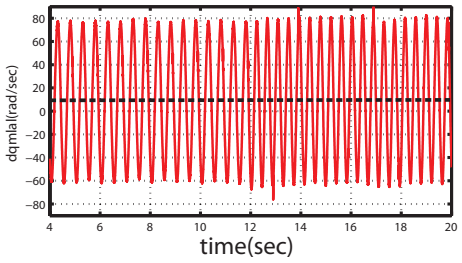


Fig. 25: Differentiated output. Mean value of the signal (dashed line) are biased.

$$y_k = a_1 y_{k-1} + b_1 u_{1,k-1} + b_2 u_{2,k-1}. \qquad (32)$$

Arranging (32) gives,

$$y_k = a_1 y_{k-1} + b_1 (u_{1,k-1} + b_2/b_1), \qquad (33)$$

where, $b_2/b_1$ is the actuator bias.

## Appendix B
## Robot Model Data

Tables VII and VIII summarize the robot parameter identified in Sections IV, V and VI. The data for the compliance is given in Table VI of Section VII-B.

TABLE VII: Mass, Center of Mass, and Moment of inertia of the links from the CAD models

| Link | Mass (kg) | Center of Mass $[r_x, r_y]$ (m) | Moment of inertia (kg·m$^2$) |
|---|---|---|---|
| Spring (Csp) | 1.8987 | [0.0009406, 0.1181] | 0.04377 |
| Torso (T) | 40.8953 | [0.01229, 0.18337] | 2.3727 |
| Cshin (Csh) | 1.6987 | [0.0004345, 0.08684] | 0.03223 |
| Thigh (Th) | 3.2818 | [0.0003110, 0.1978] | 0.1986 |
| Shin (Sh) | 1.5007 | [0.0009671, 0.1570] | 0.08813 |
| Boom | 7.2575 | [0.0, 1.48494153] | 20.4951 |

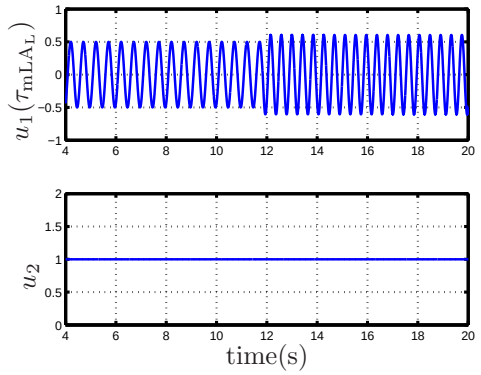


Fig. 26: $u_1$ is command input and $u_2$ is sequence of 1's which is augmented to the input signal.

TABLE VIII: Moment of inertia of the transmission pulleys

| Pulley | Moment of inertia (kg·m$^2$) |
|---|---|
| $J_{mLS}$ | 9.0144e-004 |
| $J_{\mathrm{mLA}}$ | 4.4928e-004 |
| $J_{\mathrm{Ath}}$ | 1.6680e-003 |
| $J_{\mathrm{Bth}}$ | 2.2181e-003 |
| $J_{\mathrm{Dth}}$ | 1.0826e-003 |
| $J_{\mathrm{Ash}}$ | 1.6974e-003 |
| $J_{\mathrm{Bsh}}$ | 2.2181e-003 |
| $J_{\mathrm{Dsh}}$ | 2.0542e-003 |
| $J_{\mathrm{Asp}}$ | 2.3464e-003 |
| $J_{\mathrm{Bsp}}$ | 1.8686e-003 |
| $J_{\mathrm{Dsp}}$ | 1.9313e-003 |
| $J_{\mathrm{mLSsd}}$ | 2.7117e-003 |
| $J_{\mathrm{mLAsd}}$ | 1.0950e-003 |

## APPENDIX C
## DETAILS OF THE HOPPING CONTROLLER

This section provides the details of the hopping controller used in Section VIII-B. For each phase X of Fig. 20, a simple PD control scheme is used for tracking of the controlled variables $h$ to a reference trajectory $h_{\mathrm{X}}^{ref}$:

$$u = K_p\left(h_{\mathrm{X}}^{ref} - h\right) + K_d\left(-\dot{h}\right), \tag{34}$$

where the controlled variables are

$$h := \begin{bmatrix} q_{\mathrm{LA_L}} \\ q_{\mathrm{mLS_L}} \\ q_{\mathrm{LA_R}} \\ q_{\mathrm{mLS_R}} \end{bmatrix}, \tag{35}$$

$K_p$ is a $4\times 4$ diagonal matrix of proportional gains, $K_d$ is a $4\times 4$ diagonal matrix of derivative gains, and $h_{\mathrm{X}}^{ref}$ is the desired trajectory calculated from (38)-(43) for phase X of Fig. 20. In the detailed simulation model, $h$ in (34) is quantized to the same level as the encoders on the robot, and $\dot{h}$ is obtained by numerical differentiation. The control inputs are updated with a sampling time of 1ms, which is the same as the sampling time used on the robot. Desired trajectories and transition conditions presented in (38)-(43) are calculated and checked for corresponding phase, and are inserted into (34). The following parameters are used in the trajectory calculation.

$$\mathcal{U}_d := \{\delta_{\mathrm{LA}}, h^d_{\mathrm{LS_L}}, h^d_{\mathrm{LS_R}}, \delta^-_{\mathrm{LS_L}}, \delta^-_{\mathrm{LS_R}}, \delta^+_{\mathrm{LS_L}}, \delta^+_{\mathrm{LS_R}}, h^d_{\mathrm{Tor}}\} \tag{36}$$

where $\delta_{\mathrm{LA}}$, $h^d_{\mathrm{LS_L}}$, $h^d_{\mathrm{LS_R}}$, $\delta^-_{\mathrm{LS_L}}$, $\delta^-_{\mathrm{LS_R}}$, $\delta^+_{\mathrm{LS_L}}$, $\delta^+_{\mathrm{LS_R}}$, and $h^d_{\mathrm{Tor}} \in \mathbb{R}^1$, and

$$x^d = \begin{bmatrix} x^d_1 \\ x^d_2 \\ x^d_3 \\ x^d_4 \end{bmatrix} = \begin{bmatrix} \pi - 0.5\delta_{\mathrm{LA}} - h^d_{\mathrm{Tor}} \\ \gamma_{\mathrm{LS}\to\mathrm{mLS}} h^d_{\mathrm{LS_L}} \\ \pi + 0.5\delta_{\mathrm{LA}} - h^d_{\mathrm{Tor}} \\ \gamma_{\mathrm{LS}\to\mathrm{mLS}} h^d_{\mathrm{LS_R}} \end{bmatrix}. \tag{37}$$

$$\textit{Phase I}: \begin{cases} h_{\mathrm{I}}^{ref} = \begin{bmatrix} x^d_1 \\ x^d_2 \\ x^d_3 \\ x^d_4 \end{bmatrix} \\ S_{\mathrm{I}\to\mathrm{II}} : \{p_{\mathrm{toe_L}} = 0, p_{\mathrm{toe_R}} = 0\} \end{cases} \tag{38}$$

$$\textit{Phase II}: \begin{cases} h_{\mathrm{II}}^{ref} = \begin{bmatrix} q_{\mathrm{Tor}} + q_{\mathrm{LA_R}} - h^d_{\mathrm{Tor}} - \delta_{\mathrm{LA}} \\ x^d_2 \\ q_{\mathrm{Tor}} + q_{\mathrm{LA_R}} - h^d_{\mathrm{Tor}} \\ x^d_4 \end{bmatrix} \\ S_{\mathrm{II}\to\mathrm{III}} : \{|\dot{\phi}_v| < 0.01\} \end{cases} \tag{39}$$

$$\textit{Phase III}: \begin{cases} h_{\mathrm{III}}^{ref} = \begin{bmatrix} q_{\mathrm{Tor}} + q_{\mathrm{LA_R}} - h^d_{\mathrm{Tor}} - \delta_{\mathrm{LA}} \\ x^d_2 - \gamma_{\mathrm{LS}\to\mathrm{mLS}}\delta^-_{\mathrm{LS_L}} \\ q_{\mathrm{Tor}} + q_{\mathrm{LA_R}} - h^d_{\mathrm{Tor}} \\ x^d_4 - \gamma_{\mathrm{LS}\to\mathrm{mLS}}\delta^-_{\mathrm{LS_R}} \end{bmatrix} \\ S_{\mathrm{III}\to\mathrm{IV_a}} : \{p_{\mathrm{toe_L}} > 0, p_{\mathrm{toe_R}} \le 0\} \\ S_{\mathrm{III}\to\mathrm{IV_b}} : \{p_{\mathrm{toe_L}} \le 0, p_{\mathrm{toe_R}} > 0\} \\ S_{\mathrm{III}\to\mathrm{V}} : \{p_{\mathrm{toe_L}} > 0, p_{\mathrm{toe_R}} > 0\} \end{cases} \tag{40}$$

$$\textit{Phase IV}_{\mathrm{a}}: \begin{cases} h_{\mathrm{IV_a}}^{ref} = \begin{bmatrix} H_1 h_{\mathrm{III}}^{ref}(t_{\mathrm{III}\to\mathrm{IV}}) \\ x^d_2 + \gamma_{\mathrm{LS}\to\mathrm{mLS}}\delta^+_{\mathrm{LS_L}} \\ H_3 h_{\mathrm{III}}^{ref}(t_{\mathrm{III}\to\mathrm{IV}}) \\ x^d_4 - \gamma_{\mathrm{LS}\to\mathrm{mLS}}\delta^-_{\mathrm{LS_R}} \end{bmatrix} \\ S_{\mathrm{IV_a}\to\mathrm{V}} : \{p_{\mathrm{toe_R}} > 0\} \end{cases}, \tag{41}$$

where $H_1 = [1\ 0\ 0\ 0]$, $H_3 = [0\ 0\ 1\ 0]$, and $t_{\mathrm{III}\to\mathrm{IV}}$ is the time when the transition from $III$ to $IV$ happens.

$$\textit{Phase IV}_{\mathrm{b}}: \begin{cases} h_{\mathrm{IV_b}}^{ref} = \begin{bmatrix} H_1 h_{\mathrm{III}}^{ref}(t_{\mathrm{III}\to\mathrm{IV}}) \\ x^d_2 - \gamma_{\mathrm{LS}\to\mathrm{mLS}}\delta^-_{\mathrm{LS_L}} \\ H_3 h_{\mathrm{III}}^{ref}(t_{\mathrm{III}\to\mathrm{IV}}) \\ x^d_4 + \gamma_{\mathrm{LS}\to\mathrm{mLS}}\delta^+_{\mathrm{LS_R}} \end{bmatrix} \\ S_{\mathrm{IV_b}\to\mathrm{V}} : \{p_{\mathrm{toe_L}} > 0\} \end{cases} \tag{42}$$

$$\textit{Phase V}: \begin{cases} h_{\mathrm{V}}^{ref} = \begin{bmatrix} H_1 h_{\mathrm{III}}^{ref}(t_{\mathrm{III}\to\mathrm{IV}}) \\ x^d_2 + \gamma_{\mathrm{LS}\to\mathrm{mLS}}\delta^+_{\mathrm{LS_L}} \\ H_3 h_{\mathrm{III}}^{ref}(t_{\mathrm{III}\to\mathrm{IV}}) \\ x^d_4 + \gamma_{\mathrm{LS}\to\mathrm{mLS}}\delta^+_{\mathrm{LS_R}} \end{bmatrix} \\ S_{\mathrm{V}\to\mathrm{I}} : \{t = t_{\mathrm{IV}\to\mathrm{V}} + 0.05\} \end{cases}, \tag{43}$$

where $t_{\mathrm{IV}\to\mathrm{V}}$ is the time when the transition from $IV$ to $V$ happens.

In addition to the control structure explained above, we have the following event based update of the desired torso angle for better stability:

$$\begin{aligned}\phi^*_{\mathrm{h}}[k] &= \phi_{\mathrm{h}}\left(t_{\mathrm{I}\to\mathrm{II}}\right)\\ \delta\phi_{\mathrm{h}}[k] &= \phi^*_{\mathrm{h}}[k] - \phi^*_{\mathrm{h}}[k-1]\\ \delta h^d_{\mathrm{Tor}}[k] &= K_{\mathrm{Tor}}(\delta\phi_{\mathrm{h}}[k] - \delta\phi^d_{\mathrm{h}})\\ h^d_{\mathrm{Tor}}[k] &= h^{d0}_{\mathrm{Tor}} + \delta h^d_{\mathrm{Tor}}[k],\end{aligned} \tag{44}$$

where $k$ is the hopping count, $t_{\mathrm{I}\to\mathrm{II}}$ is the time when the transition from I to II occurs, and $K_{\mathrm{Tor}}$ is the gain. Basically, this controller updates $h^d_{\mathrm{Tor}}$ based on the distance traveled horizontally during one hop. If MABEL travels less than $\delta\phi^d_{\mathrm{h}}$ during the previous hop, the torso is leaned back from the center value $h^{d0}_{\mathrm{Tor}}$, and vice versa. Adding new parameters for the update law to the parameter set, we define a new parameter set:

$$\widetilde{\mathcal{U}}_d := \{\delta_{\mathrm{LA}}, h^d_{\mathrm{LS_L}}, h^d_{\mathrm{LS_R}}, \delta^-_{\mathrm{LS_L}}, \delta^-_{\mathrm{LS_R}}, \delta^+_{\mathrm{LS_L}}, \delta^+_{\mathrm{LS_R}}, h^{d0}_{\mathrm{Tor}}, \delta\phi^d_{\mathrm{h}}\} \tag{45}$$

With the control structure explained in this section, simulation study shows that the following parameter set yields steady state dynamic hopping motion:

$$\begin{aligned}&\delta_{\mathrm{LA}} = 30^\circ,\ h^d_{\mathrm{LS_L}} = 12^\circ,\ h^d_{\mathrm{LS_R}} = 12^\circ,\\ &\delta^-_{\mathrm{LS_L}} = 5^\circ,\quad \delta^-_{\mathrm{LS_R}} = 13^\circ,\ \delta^+_{\mathrm{LS_L}} = 5^\circ,\\ &\delta^+_{\mathrm{LS_R}} = 5^\circ,\quad h^{d0}_{\mathrm{Tor}} = 8^\circ,\quad \phi^d_{\mathrm{h}} = -6.9^\circ\end{aligned} \tag{46}$$

*Acknowledgement*

The authors would like to thank J. Koncsol for his selfless dedication and help to our project. His generous sharing of the engineering experiences, and numerous contributions in the debugging of the electronic boards and design of mechanical hardware led us to successful experiments. G. Buche is gratefully acknowledged for his many contributions including the design of the electronics, power supply and safety systems. His prior experience with RABBIT was invaluable in the initial setup of the bipedal test bed.

## REFERENCES

[1] J. W. Hurst, "The role and implementation of compliance in legged locomotion," Ph.D. dissertation, Robotics Institute, Carnegie Mellon University, Pittsburgh, PA, August 2008.

[2] J. Grizzle, J. Hurst, B. Morris, H.-W. Park, and K. Sreenath, "Mabel, a new robotic bipedal walker and runner," June 2009, pp. 2030 –2036.

[3] K. Sreenath, H.-W. Park, I. Poulakakis, and J. W. Grizzle, "A compliant hybrid zero dynamics controller for stable, efficient and fast bipedal walking on MABEL," *International Journal of Robotics Research*, 2010, submitted, preprint available at [7].

[4] E. R. Westervelt, J. W. Grizzle, C. Chevallereau, J. H. Choi, and B. Morris, *Feedback Control of Dynamic Bipedal Robot Locomotion*. Taylor & Francis/CRC Press, 2007.

[5] J. Swevers, W. Verdonck, and J. D. Schutter, "Dynamic model identification for industrial robots," *Control Systems Magazine, IEEE*, vol. 27, no. 5, pp. 58 –71, Oct. 2007.

[6] J. Swevers, C. Ganseman, D. Tukel, J. de Schutter, and H. Van Brussel, "Optimal robot excitation and identification," *Robotics and Automation, IEEE Transactions on*, vol. 13, no. 5, pp. 730 –740, Oct 1997.

[7] W. Khalil and E. Dombre, *Modeling, Identification and Control of Robots*. Bristol, PA, USA: Taylor & Francis, Inc., 2002.

[8] C. G. Atkeson, C. H. An, and J. M. Hollerbach, "Estimation of inertial parameters of manipulator loads and links," *Int. J. Rob. Res.*, vol. 5, no. 3, pp. 101–119, 1986.

[9] M. Gautier and W. Khalil, "On the identification of the inertial parameters of robots," Dec 1988, pp. 2264 –2269 vol.3.

[10] P. Vandanjon, M. Gautier, and P. Desbats, "Identification of robots inertial parameters by means of spectrum analysis," vol. 3, May 1995, pp. 3033 –3038 vol.3.

[11] S. Tafazoli, P. Lawrence, and S. Salcudean, "Identification of inertial and friction parameters for excavator arms," *Robotics and Automation, IEEE Transactions on*, vol. 15, no. 5, pp. 966 –971, Oct 1999.

[12] M. Gautier and W. Khalil, "Direct calculation of minimum set of inertial parameters of serial robots," *Robotics and Automation, IEEE Transactions on*, vol. 6, no. 3, pp. 368 –373, Jun 1990.

[13] I.-J. Ha, M.-S. Ko, and S. Kwon, "An efficient estimation algorithm for the model parameters of robotic manipulators," *Robotics and Automation, IEEE Transactions on*, vol. 5, no. 3, pp. 386 –394, Jun 1989.

[14] J. Hurst and A. Rizzi, "Series compliance for an efficient running gait," *Robotics Automation Magazine, IEEE*, vol. 15, no. 3, pp. 42 – 51, september 2008.

[15] C. Chevallereau, G. Abba, Y. Aoustin, F. Plestan, E. Westervelt, C. Canudas-De-Wit, and J. Grizzle, "Rabbit: a testbed for advanced control theory," *Control Systems Magazine, IEEE*, vol. 23, no. 5, pp. 57 – 79, oct. 2003.

[16] M. H. Raibert, *Legged robots that balance*. Cambridge, MA, USA: Massachusetts Institute of Technology, 1986.

[17] J. Hurst, J. Chestnutt, and A. Rizzi, "Design and philosophy of the bimasc, a highly dynamic biped," April 2007, pp. 1863 –1868.

[18] M. A. Daley and A. A. Biewener, "Running over rough terrain reveals limb control for intrinsic stability," *Proceedings of the National Academy of Sciences*, vol. 103, no. 42, pp. 15 681–15 686, 2006. [Online]. Available: http://www.pnas.org/content/103/42/15681.abstract

[19] M. A. Daley, J. R. Usherwood, G. Felix, and A. A. Biewener, "Running over rough terrain: guinea fowl maintain dynamic stability despite a large unexpected change in substrate height," *J Exp Biol*, vol. 209, no. 1, pp. 171–187, 2006. [Online]. Available: http://jeb.biologists.org/cgi/content/abstract/209/1/171

[20] J. Hodgins and M. Raibert, "Adjusting step length for rough terrain locomotion," *Robotics and Automation, IEEE Transactions on*, vol. 7, no. 3, pp. 289 –298, Jun 1991.

[21] K. Hashimoto, Y. Sugahara, H. Sunazuka, C. Tanaka, A. Ohta, M. Kawase, H. Lim, and A. Takanishi, "Biped landing pattern modification method with nonlinear compliance control," May 2006, pp. 1213 –1218.

[22] M. Ogino, H. Toyama, and M. Asada, "Stabilizing biped walking on rough terrain based on the compliance control," 29 2007-Nov. 2 2007, pp. 4047 –4052.

[23] U. Saranli, M. Buehler, and D. E. Koditschek, "Rhex: A simple and highly mobile hexapod robot," *International Journal of Robotics Research*, vol. 20, pp. 616–631, 2001.

[24] T. Takuma, S. Hayashi, and K. Hosoda, "3d bipedal robot with tunable leg compliance mechanism for multi-modal locomotion," Sept. 2008, pp. 1097 –1102.

[25] J. W. Grizzle, "Publications on robotics," 2009. [Online]. Available: http://www.eecs.umich.edu/ grizzle/papers/robotics.html

[26] D. Marhefka and D. Orin, "Simulation of contact using a nonlinear damping model," vol. 2, Apr 1996, pp. 1662 –1668 vol.2.

[27] C. Canudas de Wit, H. Olsson, K. Astrom, and P. Lischinsky, "A new model for control of systems with friction," *Automatic Control, IEEE Transactions on*, vol. 40, no. 3, pp. 419 –425, Mar 1995.

[28] F. Plestan, J. Grizzle, E. Westervelt, and G. Abba, "Stable walking of a 7-dof biped robot," *Robotics and Automation, IEEE Transactions on*, vol. 19, no. 4, pp. 653 – 668, Aug. 2003.

[29] L. Ljung, *System identification: theory for the user*. Upper Saddle River, NJ, USA: Prentice-Hall, Inc., 1986.